

1 **Mapping snow depth within a tundra ecosystem using multiscale observations and**

2 **Bayesian methods**

3

4 Haruko M. Wainwright

5 hmwainwright@lbl.gov

6 Earth Sciences Division, Lawrence Berkeley National Laboratory

7 1 Cyclotron Road, MS 74R-316C, Berkeley, CA 94720-8126

8

9 Anna K. Liljedahl

10 akliljedahl@alaska.edu

11 Water & Environmental Research Center

12 University of Alaska Fairbanks

13 306 Tanana Loop, Fairbanks, AK 99775-5860, USA

14

15 Baptiste Dafflon

16 bdafflon@lbl.gov

17 Earth Sciences Division, Lawrence Berkeley National Laboratory

18 1 Cyclotron Road, MS 74R-316C, Berkeley, CA 94720-8126

19

20 Craig Ulrich

21 CUlrich@lbl.gov

22 Earth Sciences Division, Lawrence Berkeley National Laboratory

23 1 Cyclotron Road, MS 74R-316C, Berkeley, CA 94720-8126

24

25 John E. Peterson

26 jepeterson@lbl.gov

27 Earth Sciences Division, Lawrence Berkeley National Laboratory

28 1 Cyclotron Road, MS 74R-316C, Berkeley, CA 94720-8126

29

30 Susan S. Hubbard

31 sshubbard@lbl.gov

32 Earth Sciences Division, Lawrence Berkeley National Laboratory

33 1 Cyclotron Road, MS 74R-316C, Berkeley, CA 94720-8126

34

35 **Abstract**

36 This paper compares and integrates different strategies to characterize the variability of end-of-
37 winter snow depth and its relationship to topography in ice-wedge polygon tundra of Arctic
38 Alaska. Snow depth was measured using *in situ* snow depth probes, and estimated using ground
39 penetrating radar (GPR) surveys and the Photogrammetric Detection and Ranging (PhoDAR)
40 technique with an unmanned aerial system (UAS). We found that GPR data provided high-
41 precision estimates of snow depth (RMSE = 2.9 cm), with a spatial sampling of 10 cm along
42 transects. ~~PhoDAR-based approaches provided snow depth estimates in a less laborious manner~~
43 compared to GPR and probing while yielding a high precision (RMSE = 6.0 cm) and a fine
44 spatial sampling (4 cm by 4 cm). We then investigated the spatial variability of snow depth and
45 its correlation to micro- and macrotopography using the snow-free LiDAR digital elevation map
46 (DEM) and the wavelet approach. We found that the end-of-winter snow depth was highly
47 variable over short (several meter) distances, and the variability was correlated with
48 microtopography. Microtopographic lows (i.e., troughs and centers of low-centered polygons)
49 were filled in with snow, which resulted in a smooth and even snow surface following
50 macrotopography. We developed and implemented a Bayesian approach to integrate the snow-
51 free LiDAR DEM and multi-scale measurements (probe and GPR) as well as the topographic
52 correlation for estimating snow depth over the landscape. Our approach led to high precision
53 estimates of snow depth (RMSE = 6.0 cm), at 0.5-meter resolution and over the LiDAR domain
54 (750 m by 700 m).

Deleted: UAS

55

57 **1. Introduction**

58 Snow plays a critical role in ecosystem functioning of the Arctic tundra environment through its
59 impacts on soil hydrothermal processes and energy exchange (e.g., Callaghan et al., 2011). Snow
60 insulates the ground from intense cold during the Arctic winter, limiting the heat transfer
61 between the air and the ground (Zhang, 2005). Snow depth affects active layer and permafrost
62 temperatures throughout the year (Gamon et al., 2012; Stieglitz et al., 2003), and increased snow
63 depth has resulted in permafrost degradation (Osterkamp, 2007). Snow's insulating capacity
64 enhances conditions for active soil microbial processes and CO₂/CH₄ production during winter
65 (Nobrega and Grogan, 2007; Schimel et al., 2004; Clein and Schimel, 1995; Jansson and Taş,
66 2014; Zona et al., 2016). In addition, snow serves as an important water source to tundra
67 ecosystems during the growing season, and therefore has a large impact on biological processes
68 via hydrology. Snowmelt water can lead to extensive inundation of low-gradient tundra and large
69 runoff events in early summer (Bowling et al., 2003; Kane et al., 1991; Liljedahl et al., 2016).
70 Since soil biogeochemistry and vegetation are controlled by soil moisture (Sjögersten et al.,
71 2006; Wainwright et al., 2015), the amount of snow affects ecosystem functioning throughout
72 the season.

73

74 In order to investigate controls of snow on ecosystem properties, high resolution estimates of
75 snow are needed over large spatial regions. This is especially true in ice-wedge polygon tundra,
76 which dominates a large portion of the high Arctic (Zona et al., 2011). The ice wedges develop
77 when frost cracks occur in the ground, and vertical ice wedges grow laterally over years
78 (Leffingwell, 1915; MacKay, 2000). Soil movement associated with ice-wedge development
79 creates small-scale topographic variations → microtopography → where the ground surface

Deleted: s

Deleted: s

Deleted: Polygon evolution – caused by successive freezing, cracking and thawing of soil and ice and associated movement of soil – leads to

Deleted: ,

86 elevation can vary significantly over lateral length distances of several meters (e.g., Brown,
87 1967; MacKay, 2000; Engstrom et al., 2005; Zona et al., 2011). This microtopography leads to
88 dramatically variable snow depth across short distances. Liljedahl et al. (2016) found that the
89 differential snow distribution increased the partitioning of snowmelt water into runoff, leading to
90 less water stored on the tundra landscape. Gamon et al. (2012) reported that snow depth
91 heterogeneity results in differential thawing and active layer thickness variability. In addition,
92 there is large-scale topographic variability at the scale of several hundred meters to kilometers,
93 macrotopography, which is often associated with drained thaw lake basins or drainage features
94 (Hinkel et al., 2003). Although the effect of macrotopography on snow depth has not been
95 studied, Engstrom et al. (2005) quantified that both macrotopography and microtopography have
96 a significant effect on soil moisture distribution. The snow representation of the Arctic tundra
97 needs to be refined to account for the effect of such multiscale terrain heterogeneities on
98 hydrology and ecosystem functioning, by bridging between finer geographical scales (several
99 meters) and large areal coverage (several hundred meters to kilometers).

100

101 Snow depth characterization in Arctic tundra environments has traditionally been performed
102 using snow depth probes (Benson and Sturm, 1993; Hirashima et al., 2004; Derksen et al., 2009;
103 Rees et al., 2014; Dvornikov et al., 2015), or modeled using terrain and vegetation information
104 (Sturm and Wagner, 2010; Liston et al., 1998; Pomeroy et al., 1997). Recently, there have been
105 several new techniques for estimating snow depth in high resolution, and in a non-invasive and
106 spatially extensive manner. Ground-penetrating radar (GPR) has been widely used to
107 characterize snow cover in alpine, arctic and glacier environments (e.g., Harper and Bradford,
108 2003; Machguth et al., 2006; Gusmeroli and Grosse, 2012; Gusmeroli et al., 2014). GPR

Deleted: are

Deleted: spatial

Deleted: in ground surface elevation

Deleted: , or

Deleted: , which can vary over lateral distances of several hundred meters to kilometers; m

Deleted: acrotopography

Deleted: s

Deleted: T

Deleted: the snow representation of the Arctic tundra needs to be refined, especially

Deleted: from

Deleted: sub-meter

Deleted: to

Deleted: ave

Deleted: observed

Deleted: In the tundra environment, snow depth characterization has been limited to ground-based point (probe) measurements (Benson and Sturm, 1993; Dvornikov et al., 2015).

129 measures the radar reflection from the snow-ground interface, which can be used to estimate
130 snow depth. GPR can be collected by foot, snowmobile or airborne methods. In addition, Light
131 Detection and Ranging (LiDAR) and Photogrammetric Detection and Ranging (PhoDAR)
132 airborne methods have recently been used to estimate snow depth at local and regional scales
133 (e.g., Deems et al., 2013; Harpold et al., 2014; Nolan et al., 2015). Both techniques measure the
134 snow surface elevation, using laser in LiDAR, or a camera with a structure-from-motion (SfM)
135 algorithm in PhoDAR. Both approaches allow us to estimate snow depth by subtracting the
136 snow-free elevation from the snow surface elevation. While there is potential for providing
137 detailed information about local-scale snow variability using LiDAR and PhoDAR snow depth
138 estimates, these techniques have not been extensively tested in ice-wedge-polygonal tundra
139 environments.
140
141 Such indirect geophysical methods are, however, known to have increased snow depth
142 uncertainty relative to direct measurements (here ground-based snow depth probe measurements)
143 (e.g., Hubbard and Rubin, 2005). The uncertainty of the snow depth probe measurements is sub-
144 centimeter to several centimeters depending on the surface vegetation (Berezovskaya and Kane,
145 2007). On the other hand, the snow depth estimates obtained using GPR can be affected by
146 uncertainty associated with radar velocity, which depends on snow density (Harper and
147 Bradford, 2003). In the environments with complex terrain such as ice-wedge polygonal tundra,
148 GPR-based snow estimates could also be influenced by the errors stemming from radar
149 positioning and raypath assumptions. The airborne LiDAR/PhoDAR-based methods are subject
150 to the errors associated with georeferencing, processing and calibration (e.g., Deems et al., 2013;

Deleted: the snow and ground surface

Deleted: h

Deleted: site

Deleted: or

Formatted: English (US)

Deleted: and

Deleted: the

Deleted: , which

Deleted: s

Deleted: While the potential of those advanced methods for providing information about snow variability has been documented, they have not been used extensively for characterizing the variability of snow depth in ice-wedge polygonal tundra

Deleted: increased uncertainty

Deleted: For example, t

166 Nolan et al., 2015). The accuracy of the airborne methods is usually several tens of centimeters,
167 which is lower than the snow depth probe measurements.

Deleted: the centimeter accuracy of

168
169 Integrating different types of snow measurements can take advantage of the strengths of various
170 techniques while minimizing the limitations stemming from using a single method. Bayesian
171 approaches have proven to be useful for integrating multiscale, multi-type datasets to estimate
172 spatially heterogeneous terrestrial system parameters in a manner that honors method-specific
173 uncertainty (e.g., Wikle et al., 2001; Wainwright et al., 2014; 2016). Bayesian methods also
174 permit systematic incorporation of expert knowledge or process-specific information, such as the
175 relationships between datasets and parameters. In particular, snow depth is known to be affected
176 by topography and wind direction (e.g., Benson and Sturm, 1993; Anderson et al., 2014;

177 Dvornikov et al., 2015). To our knowledge, such Bayesian data integration methods have never
178 been applied to estimate end-of-winter snow variability using multiple types of datasets.

Deleted: integration

Deleted: not

Deleted: developed

179
180 The primary objectives of this study are to (1) compare point-scale snow depth probe, GPR and
181 UAS-based PhoDAR approaches for characterizing snow depth, and the associated resolution
182 and accuracy of the GPR and PhoDAR methods; (2) quantify the spatial variability of end-of-
183 winter snow depth in ice-wedge polygonal tundra landscape; (3) explore the relationship between
184 snow depth and topography; and (4) develop a Bayesian method to integrate multiscale, multi-
185 type data to estimate snow depth over a LiDAR DEM covering an ice-wedge polygonal tundra
186 landscape. In Section 2, we describe our site and datasets, including snow depth probes, ground-
187 based GPR and UAS-based PhoDAR. In Section 3, we present the methodology to analyze the
188 indirect snow depth measurements from GPR and PhoDAR as well as to evaluate the

Formatted: Tabs: 0.2", Left + 3.2", Centered + 6.5", Right

Deleted: UAS

Deleted: characterize

Deleted: heterogeneity

Deleted: the LiDAR domain

Deleted: point

198 heterogeneity of snow depth in relation to both microtopography (i.e., ice-wedge polygons) and
199 macrotopography (i.e., large-scale gradient, drained thaw lake basins and interstitial upland
200 tundra). We then develop a Bayesian geostatistical approach to integrate the multiscale datasets
201 to estimate snow depth over the LiDAR domain. The snow measurement and estimation results
202 are presented in Section 4 and discussed in Section 5.

Deleted: .

204 **2. Data and Site Descriptions**

205 **2.1. Study Site**

206 Snow survey data were collected within a study site (approximately 750 m by 700 m) located on
207 the Barrow Environmental Observatory near Barrow, Alaska, as part of the Department of
208 Energy's Next-Generation Ecosystem Experiment (NGEE) Arctic project (Figure 1). This study
209 domain has been characterized intensively in the NGEE-Arctic project, leading to various
210 ecosystem and subsurface datasets, including snow depth measurements (Wainwright et al.,
211 2015; Dafflon et al., 2016). Mean annual air temperature at the Barrow site is -11.3°C and mean
212 annual precipitation is 173 mm (Liljedahl et al., 2011). Snowmelt usually ends in early to mid-
213 June. The wind direction is predominantly from east to west throughout the year.

Deleted: , and produced

214
215 Ice-wedge polygons are prevalent in the region, including low-centered polygons in drained thaw
216 lake basins and high-centered polygons with well-developed troughs in the upland tundra
217 (Hinkel et al., 2003; Wainwright et al., 2015). The dominant plants are mosses (*Dicranum*
218 *elongatum*, *Sphagnum*), lichens and vascular plants (such as *Carex aquatilis*); plant distribution
219 at the site is governed by surface moisture variability (e.g., Hinkel et al., 2003; Zona et al.,
220 2011). There are currently no tall shrubs or woody plants established within the study site,
221 therefore complex topography is most likely to control the snow depth distribution within the
222 study domain. (Sturm et al., 2005; Dvornikov et al., 2015).

Deleted: There are no shrubs or tall woody plants that are known to affect snow depth

223
224 Three long transects and four representative plots were chosen within the study site to explore
225 snow variability and its relationship to topography (Figure 1). Typical for low-gradient tundra
226 terrain, ice-wedge polygon microtopographic variations are superimposed on macrotopographic

230 trends at the study site. The elevation is higher in the center of the domain (interstitial upland
231 tundra) and lower near the drainage features in the south. The elevation is also relatively lower in
232 the drained thaw lake basins (DTLB) region, which is located in the northeastern and
233 northwestern edges of the study site. The four intensive plots (A-D), each 160m x 160m, were
234 chosen to represent specific polygon types or macrotopographic positions within the study area.

235 ~~The three parallel transects, each ~500m long, were designed to traverse multiple polygon types~~
236 ~~in a continuous fashion (Hubbard et al., 2013). We refer to those transects by “the 500-meter~~
237 ~~transects”.~~

Deleted:

239 2.2. Datasets

240 Airborne LiDAR data were collected at the site on October 4th, 2005, ~~and used to provide a~~
241 ~~high-resolution digital elevation map (DEM) of the snow-free ground at 0.5 m by 0.5 m~~
242 ~~resolution (Hubbard et al., 2013). The DEM effectively resolves both micro- and~~
243 ~~macrotopography at the study site (Figure 1). The original reported accuracy is 0.3 m in the~~
244 ~~horizontal direction and 0.15 m in the vertical direction.~~ To evaluate the accuracy of the airborne
245 DEM, we measured the ground surface elevation in September 2011 ~~at 1286 points around the~~
246 ~~500-meter transects,~~ using a high-precision centimeter-grade RTK Differential GPS (DGPS)
247 system ~~(the reported precision about 2 cm in the horizontal direction and 3 cm in the vertical~~
248 ~~direction).~~ The root mean square error of the LiDAR DEM compared to ~~the GPS data~~ was
249 6.08 cm.

Deleted: ing

Deleted: d

Deleted: .

Deleted: The precision of the RTK DGPS is estimated to be about 2 cm in direction and 3 cm in direction.

251 The majority of the snow depth data was collected on May 6–12, 2012, during which no snowfall
252 occurred and little change in snow depth was observed. Snow depth was measured in the four

259 intensive study plots and along three transect lines (Figure 1). Two sets of snow depth
260 measurements using a snow depth probe were collected. The ‘fine-grid’ dataset was aimed to
261 characterize the fine-scale heterogeneity by ~7200 snow depth point measurements (every
262 ~0.3 m along transects with a 4 m spacing) across a small domain (~50 × 50 m) within Plots A-

263 D. This was done using a GPS snow depth probe (Magnaprobe by Snow-Hydro) which had a
264 reported vertical precision of < 0.01 m and horizontal precision of around 0.5 m. The corner
265 coordinates within each grid were surveyed with the RTK DGPS, while each snow depth point
266 measurement was represented by the built-in GPS unit that was programmed to automatically
267 record locations. All the snow depth point measurements were made along regularly spaced
268 transects. Comparisons between coordinates surveyed with both the RTK DGPS and the built-in
269 GPS confirmed constant biases in the horizontal directions, which allowed a constant bias
270 adjustment for all GPS surveyed snow depth point measurements.

271
272 A second ‘coarse-grid’ set of snow depth measurements covered the entire area in Plots A-D
273 (~160 m × 160 m) with lower sampling density. The coarse-grid snow data were collected using

274 a tile probe, which had a precision of approximately 0.01 m. Snow depth was measured every
275 8 m along a measurement tape along five parallel transects in the coarse grid, which were spaced
276 40 m apart. The total number of data points was 380 (95 points in each plot). Along the 500-
277 meter transects, we used the tile probe along with a measurement tape, and measured eight
278 points along each of the three lines. The start and end coordinates of each transect were surveyed
279 with a RTK DGPS and used to georeference the measurement locations.

Deleted: th
Deleted: . The
Deleted: accuracy
Deleted: this snow probe was

Deleted: . The start and end coordinates of each transect were surveyed with a RTK DGPS and used to correct point measurement locations in respective transect.

Deleted: tile
Deleted: n
Deleted: accuracy
Deleted: 5
Deleted: set
Deleted: lines
Deleted: in each plot
Deleted: approximately

296 Ground-based ground penetrating radar (GPR) data were acquired over the four study plots and
297 along the three 500-meter transects. The instrument (Mala ProEx with 500 MHz antenna) was
298 pulled on a sled. In each plot, we acquired the GPR data at 0.1-m intervals (triggered by an
299 odometer wheel) along 37 lines of 4-m spacing. The start and end coordinates of each transect
300 were surveyed with a RTK DGPS and used to georeference the measurement locations. We
301 compared the distance from wheel with the distance on tape and confirmed that the difference is
302 generally very small at this site. The error of horizontal positioning is estimated to be about 0.1
303 m. Several of the GPR lines were co-located with the 'coarse-grid' snow depth probe
304 measurements. The GPR technique allowed for denser sampling within the plot relative to the
305 snow depth probe, with more than 50,000 points in each plot. Due to the microtopography at this
306 site, the positioning errors between in situ measurements and GPR data could lead to an error in
307 the radar velocity and snow depth estimation. We evaluate the effect of such positioning errors
308 extensively, as described in Section 3.1.

309
310 The GPR reflection signal from the bottom of snowpack (i.e., the ground surface) was clear,
311 which allowed us to measure the travel time between the top and bottom of snowpack. The GPR
312 processing routine consisted of (1) zero-time adjustment, (2) average tracer removal, (3) picking
313 the travel time (manually with automated snapping in the ProMAX® software) of the reflected
314 GPR signal that travelled from the snow surface to the snow-ground interface and back to the
315 snow surface and (4) dividing by two to obtain a one-way travel time between the snow surface
316 and ground surface. We processed the GPR data including travel-time picking before accounting
317 for topography. More details on GPR processing and theory can be found in Annan (2015) and
318 Jol (2009), while more detailed explanation on the use of GPR in the tundra can be found in

Deleted: G

Deleted: marked

Formatted: Font color: Text 1

Deleted: precision

Deleted: in

Deleted: of the measurements

Deleted: tile

Deleted: , while the exact location of each measurement was within ~1 m (marked by tape majors)

Deleted: data were pre-processed to maximize signal-to-noise ratio; a detailed explanation of the use and processing of GPR at this study site was provided by Hubbard et al. (2013). Our pre-

Deleted: picking the airwave (which is used to define the signal initiation time, or 'zero time')

Deleted: 2

Deleted: reflection

Deleted: of the

Deleted:

Deleted: , (3) subtracting the zero time from the reflection pick

Formatted: Font color: Text 1

Deleted: A more detailed explanation on the use of

Deleted: various review papers

Deleted: () and

Formatted: Font color: Text 1

Formatted: Font color: Text 1

342 Hubbard et al. (2013). Differing from previous studies (e.g., Harper and Bradford, 2003), we did
343 not observe echoes from snow layering. This is possibly because of the low antenna frequency
344 (500 MHz), relatively thin snow layers (if present), and the low contrast between various snow
345 layers. In addition, hoar layers or ice layers were not visible in our data or sensed using the
346 probe. Although ice may form at the ground surface, causing the uncertainty of a few
347 centimeters, we did not consider this effect in this study.

348

349 Additional campaigns were carried out in 2013 – 2015 along the 500-meter transects only. UAS-
350 based PhoDAR data were collected in July 2013 and 2014 to estimate snow-free ground surface
351 elevation and in May 2015 for estimating snow depth along the transects. To make these
352 measurements, we lifted a consumer-grade digital camera (Sony Nex-5R) to about 40 meters
353 above the ground surface using a kite, and acquired downward-looking Red-Green-Blue
354 landscape images, as well as collected some surface elevation data (method described in Smith et
355 al., 2009). The reconstruction procedure was performed using a commercial computer vision
356 software package (PhotoScan from Agisoft LLC). Reconstruction involved automatic image
357 feature detection/matching, structure-from-motion and multiview-stereo techniques for 3D point-
358 cloud generation, and georeferenced mosaic reconstruction (Nolan et al., 2015). High-accuracy
359 georeferencing was enabled by using a network of ground control points placed on the ground
360 (in summer) and on the snow (in winter) that were surveyed with a high-precision centimeter-
361 grade RTK DGPS system. The reconstructed PhoDAR surface elevation models at this site show
362 a resolution of 4 cm by 4 cm. We investigated the accuracy in detail as described in Section 3.2.

363

Deleted: 2014 and

Deleted:

Deleted: only

Deleted: and

368 The snow-free ground surface elevation measurements were then subtracted from the snow
369 surface data to estimate the snow depth over the area. The snow depth probe measurements were
370 taken at 183 locations along one of the 500-meter transects to validate the PhoDAR-based snow
371 depth estimates. The locations were marked on a measurement tape, the start and end coordinates
372 of which were surveyed with a RTK DGPS and used to georeference the measurement locations.

Formatted: Line spacing: double, Tabs: 0.2", Left + 3.2", Centered + 6.5", Right

Deleted: UAS-based

Deleted: measure

Deleted: For the probe measurements,

Deleted: the transect

Deleted: .

378 **3. Methodology**

379 **3.1. GPR Snow Depth Analysis**

380 Snow depth can be inferred by multiplying GPR one-way travel time by radar velocity. The radar
381 velocity is determined by the dielectric constant, which depends on snow density in dry snow

382 (Tiuri, et al., 1984; Harper and Bradford, 2003). Depending on site conditions, the snow density
383 can vary in both vertical and horizontal directions (Proksch et al., 2015). In this study, we
384 assume that the depth-averaged radar velocity—which is a function of depth-averaged snow
385 density—is sufficient for estimating snow depth. Thus, we compute the radar velocity based on
386 the known snow depth from co-located snow depth probe measurements as: (radar velocity) =
387 (probe-based snow depth)/(GPR one-way travel time). In addition, we investigate whether the
388 lateral variations in snow density are significant at our site.

389
390 Identifying co-located points between the GPR and snow depth probe measurements, however, is
391 not a trivial task in polygonal ground, since the topography and snow depth can vary

392 significantly within a meter. To address these issues, we investigate the correlations between the
393 radar velocity and the submeter-scale variability of topography. To link the DEM elevation data
394 to the snow depth probe and GPR data, we selected the DEM elevation (0.5 m by 0.5 m
395 resolution) and GPR measurement at the nearest locations to the tile probe measurements. We
396 assume that the effect of positioning errors is larger near the edge of polygons, or in the region
397 where the submeter-scale topographic variability is high. We consider that the uncertainty of
398 radar velocity can be reduced by not using the co-located snow depth probe measurements in
399 regions of high submeter-scale variability. To define the submeter-scale variability, we compute
400 the elevation difference within a 1-meter radius of each snow depth probe measurement. In

Deleted: the studied site

Deleted: T

Deleted: significantly or not, this

Deleted: could be variable

Deleted: /or

Deleted: Although the snow density is known to be variable in a vertical direction, we assume that

Deleted: in this study

Deleted:

Deleted: Further

Deleted: the accuracy in snow depth estimations to evaluate if

Deleted: potential lateral variations

Deleted: need to be accounted or not

Deleted: ; , while uncertainty is present in every acquisition method and inand georeferencing both lead to uncertainty..

Deleted: topographic

Deleted: topographic

420 addition, the reflections from the troughs could originate from the edge of polygons rather than
421 the location right below the GPR instrument. Such an “edge reflection” effect can lead to
422 overestimation of the radar velocity. We assume that we could detect the presence of the edge
423 reflection by evaluating the systematic bias (i.e., underestimation) in the radar velocity in relation
424 to the submeter-scale topographic variability.

Deleted:

426 3.2. UAS-based PhoDAR Snow Depth Analysis

Deleted: UAS

427 We first evaluate the accuracy of the PhoDAR-derived digital surface model (DSM) by
428 comparing it to the RTK GPS elevation measurements along the 500-meter transects acquired in
429 2011. Since the PhoDAR-derived DSM was obtained at very high lateral resolution (4 cm by 4
430 cm), it was more prone to noise or small-scale variability (Nolan et al., 2015). As such, we test
431 three schemes to explore the vertical agreement between the two datasets: (1) nearest points, (2)
432 average elevation within the 0.5-m radius, and (3) minimum elevation within the 0.5-m radius.

Deleted: UAS

Deleted: UAS

Deleted:

Deleted: co-location

433 We used the same scheme (the best scheme among the three) for determining the snow-free and
434 snow surface elevation at the co-located points. We then compare the snow depth estimate from
435 PhoDAR and snow depth probe measurements at co-located points (the May-2015 snow data). In
436 the same manner as the GPR data, we eliminate the snow depth probe measurements in the
437 regions where the submeter-scale topographic variability is high.

Deleted: UAS

439 3.3. Spatial Variability Analysis of Topography and Snow Depth

440 To quantify the topographic effects in a complex terrain of ice-wedge polygons and to partition
441 micro- and macrotopography, we apply the wavelet transform method to the airborne LiDAR
442 DEM, which is commonly used for 2D image processing. The wavelet approach has been

Deleted: recently

451 applied to DEM for geomorphic studies, including terrain analysis and landslide analysis (Bjørke
452 and Nilsen, 2003; Kalbermatten, 2010; Kalbermatten et al., 2012). In this transform, a high-pass
453 filter (a mother wavelet) and a low-pass filter (a father wavelet) are applied to decompose the
454 DEM into four images at each scale: low-pass, high-pass horizontal, high-pass vertical, and high-
455 pass diagonal images). The scale is a parameter in the wavelet transform, representing the width
456 of the filter and the scale of topographic variability (Kalbermatten et al., 2012). Depending on
457 the scale of the wavelet transform, the method yields different images, corresponding to different
458 scales of topographic features. We define this wavelet scale as a *topography separation scale*.
459 We consider the low-pass image as *macrotopographic elevation* (i.e., the smoothed version of
460 the original DEM) and the high-pass diagonal image as *microtopographic elevation* (i.e., the
461 topographic variability associated with ice-wedge polygon development). Removing the large-
462 scale topography has been done in the previous studies in order to capture or quantify the effect
463 of microtopography on carbon fluxes (Wainwright et al., 2015) or soil properties (Gillin et al.,
464 2015).
465
466 Correlations between the topographic metrics and snow depth are identified using the Pearson
467 product-moment correlation coefficient (Anderson et al., 2014). At each spatial scale, we can
468 compute micro- and macrotopographic metrics such as slope and curvature as well as their
469 correlations with corresponding probe-measured snow depth. The curvature is of particular
470 interest, since Dvornikov et al. (2015) reported strong correlations between snow surface
471 curvature and snow depth, and a dependency of this correlation on the DEM resolution (the
472 lower resolution led to lower correlation coefficients). Note that the DEM resolution (0.5 m) in
473 this study is much finer than the one (25 m) in Dvornikov et al. (2015). We compute a wind

474 factor in a similar manner as Dvornikov et al. (2015), with a slight modification. Here we define
475 the wind factor as the inner product of the slope direction and predominant wind direction. With
476 this calculation, the wind factor is smallest in the slope against the wind direction, and largest in
477 the slope in line with the wind, which is reasonable and also consistent with visual observations
478 at the site. When the correlation is statistically significant, the metrics are included in a
479 regression analysis (Davison, 2003) to represent the snow depth as a function of the topographic
480 metrics.

481
482 A geostatistical approach has been used to investigate the spatial variability of snow depth as
483 well as the scales of variability (Anderson et al., 2014). The standard geostatistical analysis starts
484 with creating an empirical variogram, followed by estimating the spatial correlation parameters
485 (Diggle and Ribeiro, 2007). The spatial correlation parameters include (1) magnitude of
486 variability (or spatial heterogeneity) as variance, (2) fraction of correlated and uncorrelated
487 variability (nugget ratio), (3) spatial correlation length (range), and (4) covariance model (i.e.,
488 the shape of decay in the spatial correlation as a function of distance), such as exponential and
489 spherical models. The covariance models (equivalent to variogram models) can be selected to
490 minimize the weighted sum of squares during variogram fitting.

491
492 ~~Such spatial variability and correlation are particularly important for interpolating the sparse in~~
493 ~~situ snow depth measurements.~~ The interpolation can be applied not only for snow depth itself
494 but also for snow surface (snow depth plus elevation) or residual snow depth after removing
495 topographic correlations in the regression analysis. The same geostatistical analysis ~~method is~~

Deleted:

Deleted: interpolating the sparse snow depth measurements

Deleted: are

500 therefore performed for snow surface and residual snow depth. [We used the geoR package in](#)
501 [statistical software R \(Ribeiro and Diggle, 2001; https://www.r-project.org/\).](#)

502

Deleted: .

503 3.4. Bayesian Geostatistical Estimation Method

504 We first define that the snow depth at each pixel y_i ($i = 1, \dots, n$) is a hidden variable which can be
505 observed only with an added measurement error. In this study, we set the pixel size to 0.5 by
506 0.5 m, which corresponded to the LiDAR DEM resolution. The snow depth distribution (or field)

507 is defined by a vector $\mathbf{y} = \{y_i | i = 1, \dots, n\}$. We integrate three datasets: [snow depth probe data \$\mathbf{z}_p\$,](#)

Deleted: point-

508 GPR data \mathbf{z}_g , and LiDAR DEM \mathbf{z}_d . The goal of the estimation is to determine the posterior
509 distribution of snow depth conditioned on all the given datasets, $p(\mathbf{y} | \mathbf{z}_p, \mathbf{z}_g, \mathbf{z}_d)$. Following a
510 Bayesian hierarchical approach, we divide this posterior distribution into three sets of statistical
511 sub-models (Wikle et al., 2001; Wainwright et al., 2014; 2016). First, *data models* represent each
512 data value as a function of snow depth at each pixel, depending on different data types. Second,
513 *process models* describe the spatial distribution of snow depth (i.e., snow depth field) as function
514 of topography and correlation parameters. Finally, *prior models* define the prior information of
515 parameters. The hierarchical approach breaks down a complex posterior distribution into a series
516 of simple models, and hence enables us to capture complex relationships easily. In addition to
517 the snow field vector and data vectors, two parameter vectors are defined: the process-model
518 parameter vector \mathbf{a} to represent the heterogeneous pattern of snow depth, and the data-model
519 parameter vector \mathbf{b} to describe the correlations between the snow depth and the GPR travel time.

520

521 We assume a linear model to describe the snow depth field,

$$522 \quad \mathbf{y} = \mathbf{A}\mathbf{a} + \boldsymbol{\tau} \quad (1)$$

525 where A is the design matrix as a function of the topographic metrics as explanatory variables
526 (and hence a function of DEM z_d). The process-model parameter vector \mathbf{a} describes the
527 correlation between the topographic metrics and the snow depth field. We assume that the
528 residual of this correlation $\boldsymbol{\tau}$ represents the unexplained variability by the topographic metrics
529 and that $\boldsymbol{\tau}$ is spatially correlated. The residual term $\boldsymbol{\tau}$ is described by a multivariate normal
530 distribution with a covariance Σ , which is determined by a geostatistical analysis (Diggle and
531 Ribeiro, 2007). Although we may include the uncertainty of those geostatistical parameters in the
532 Bayesian estimation (Diggle and Ribeiro, 2007; Lavigne et al., 2016), we assume that those
533 parameters are fixed during the Bayesian estimation process in this study. This is because we
534 have a large amount of point measurements (snow depth probe data), and also it is known that
535 indirect information (such as geophysics) does not significantly improve the estimation of
536 geostatistical parameters (Day-Lewis, 2004; Murakami et al., 2010).

537
538 The data model for the snow depth probe measurements defines the snow depth probe data z_p as
539 a function of snow depth y :

$$z_p = y + \varepsilon_p \quad (2)$$

541 We assume that the vector $\boldsymbol{\varepsilon}_p$ is an uncorrelated normally-distributed measurement error at each
542 data location with the standard deviation of σ_p . We determine the error based on the precision
543 estimate of each snow depth probe. The snow depth probe data vector z_p follows a multivariate
544 normal distribution with the mean vector \mathbf{y} and the covariance matrix D_p , which is a diagonal
545 matrix with diagonal elements of σ_p^2 . Although it is not considered this study, we could include a
546 systematic bias of snow probe measurements as an added shift (Berezovskaya and Kane, 2007).

Deleted: accuracy

Deleted: with

550 The data model for the GPR data describes the GPR data z_g as a function of the snow depth y at
551 the GPR locations. The GPR data model can be represented by a linear model:

$$552 \quad z_g = b_0 + B\mathbf{y} + \boldsymbol{\varepsilon}_g \quad (3)$$

553 where B is a matrix, the diagonal elements of which is b_1 . The error vector $\boldsymbol{\varepsilon}_g$ is an uncorrelated
554 normally-distributed measurement error with the standard deviation of σ_g . The standard
555 deviation is computed from comparing the GPR-based snow depth to the probe-based one. At the
556 same time, the GPR data model can be written as a function of the parameter vector \mathbf{b} such that:

$$557 \quad z_g = Y\mathbf{b} + \boldsymbol{\varepsilon}_g \quad (4)$$

558 where Y is the design matrix with the first column being y , and the second column being all one.
559 The parameter vector $\mathbf{b} = \{b_1, b_0\}$ represents the linear correlations between the GPR data and
560 snow depth. This alternative model is useful during the estimation procedure described below.

561 The GPR data vector z_g follows a multivariate normal distribution with the mean vector \mathbf{y} and the
562 covariance matrix D_g that is a diagonal matrix with diagonal elements of σ_g^2 .

563

564 The posterior distribution of the snow depth conditioned on the datasets $p(\mathbf{y} | z_d, z_p, z_g)$ is a
565 marginal distribution of $p(\mathbf{y}, \mathbf{a}, \mathbf{b} | z_d, z_p, z_g)$. By applying Bayes's rule and following the
566 conditional dependencies defined above, we can decompose this posterior distribution as:

$$567 \quad p(\mathbf{y}, \mathbf{a}, \mathbf{b} | z_d, z_p, z_g) \propto p(z_g | \mathbf{y}, \mathbf{b}) p(z_p | \mathbf{y}) p(\mathbf{y} | \mathbf{a}, z_d) p(\mathbf{a}) p(\mathbf{b}). \quad (5)$$

568 Table 1 defines all the distributions on the right-hand side of Equation (5) based on the models
569 defined in Equations (1) – (4). We also assume multivariate normal distributions for the prior
570 distributions of the parameter vectors \mathbf{a} and \mathbf{b} . The posterior distribution in Equation (5) can be
571 computed using the Markov-chain Monte-Carlo (MCMC) method (Gamerman and Lopes, 2006).
572 Since all the distributions are defined as multivariate normal distributions, it is possible to use

Deleted: with

Formatted: English (US)

Formatted: Line spacing: double

574 efficient Gibbs' algorithm. The MCMC procedure is described in Appendix A. The convergence
575 can be confirmed by the Geweke's convergence diagnostic (Geweke, 1992). The entire workflow
576 is included in Appendix B.

Deleted: -

578 **4. Results**

579 **4.1. Snow Depth Measurements**

580 **GPR Radar Velocity Analysis**

581 Our results (based on the GPR data and tile probe data collected in May 2012) indicate that the
582 estimated radar velocity itself does not have a systematic dependency on (or trend with) the snow
583 depth or submeter-scale variability of topography in May 2012 (Figures 2a and 2b). The
584 correlation coefficient between the radar velocity and snow depth is 0.11, and between the radar
585 velocity and submeter-scale variability is 0.15. The variability of the radar velocity, on the other
586 hand, depends on those two factors (i.e., the variability of snow depth and topography). Hence,
587 the variability is higher in areas with shallower snow depths (Figure 2a). The standard deviation
588 (STDEV) of the radar velocity is 0.039 m/ns at the snow depth smaller than one STDEV minus
589 the median snow depth, and 0.019 m/ns at the one larger than one STDEV plus the median. The
590 radar velocity variability is higher also in localized regions of large submeter-scale topographic
591 variability (Figure 2b). The STDV of the radar velocity is 0.015 m/ns at the submeter-scale
592 topographic variability (i.e. elevation difference within a one-meter radius) smaller than 0.05 m,
593 and 0.036 m/ns at the one larger than 0.05m. By selecting the points with the submeter-scale,
594 topographic variability < 0.05 m, we obtained a mean radar velocity of 0.25 m/ns, which was
595 used for subsequent analysis.

596

597 Using the mean velocity value in May 2012, the calculated GPR-based snow depth estimates
598 were compared with the snow depth probe measurements (Figure 2c). The correlation between
599 the measured and estimated snow depth is high (the correlation coefficient is 0.88), with the root
600 mean square error (RMSE) being 5.4 cm, and with no significant under- or overestimation (the

Comment [Office2]: Comment R2-(1)

Comment [Office3]: Comment R2-(1)

Deleted: topographic

Deleted: snow

Deleted: depth

Deleted: the one

Deleted: the

Deleted: snow depth

Deleted: the one of

Deleted: T

Deleted: at

Deleted: , and also

Deleted: a

Comment [Office5]: Comment R2-(1)

612 mean bias error -0.16 cm). The selected points in the regions of low submeter-scale topographic
613 variability (red circles) are more tightly distributed around the one-to-one line. In these regions,
614 the RMSE of GPR-based snow depth improved to 2.9 cm with a increased correlation coefficient
615 between the GPR-based and probe-based snow depth, to 0.94. These results confirm that snow
616 density variations are limited, and using a constant mean GPR velocity is acceptable.

- Deleted: . The
- Deleted:
- Deleted: increase
- Deleted: was
- Deleted: increased
- Deleted:
- Deleted: in snow density is
- Deleted: that
- Deleted:

618 *Snow Depth Measurements in Different Polygon Types*

619 Figure 3 shows the LiDAR DEM as well as snow depth probe measurements and GPR estimates
620 in Plots A–D (May 2012). The LiDAR DEM (in the left column) illustrates the difference among
621 four plots in terms of both macro- and microtopography. For example, Plot A has better defined
622 polygon rims and troughs than Plot D, although Plot A and D are both low-centered polygons.
623 Plot B has round-shaped high-centered polygons, while Plot C has flat-centered polygons with
624 well-defined troughs. The average size of polygons is also different, with smaller polygons in
625 Plot B and larger polygons in Plots A, C and D. In addition, these figures illustrate some
626 macrotopographic trends. Plot C is gradually sloping down towards the east, and Plot D has a
627 depression (i.e., DTLB) in the northeastern half.

Comment [Office6]: Comment R2-(1)

628
629 The middle column in Figure 3 shows the snow depth probe data collected using the fine-grid
630 and coarse-grid scheme collected in May 2012. The fine-grid data reveals the detailed
631 heterogeneity of snow depth around a single polygon. For example, the fine-grid data in Plot A
632 show the snow depth distribution in a low-centered polygon, including thin snow along the
633 polygon rim and thick snow at the polygon center and trough. Comparison of the fine-grid snow
634 data with the DEM reveals the microtopographic effect such that the troughs and center of the

Comment [Office7]: Comment R2-(1)

- Deleted: that
- Deleted: they are mirror images of each other

646 polygon have larger snow depth. The coarse-grid dataset covers the entire plot, although it is
647 much more difficult to ascertain the relationship between the snow depth and microtopography.
648 The snow depth probe data show that the snow depth is highly variable, ranging from 0.2 m to
649 0.8 m in a single plot.

650
651 In the third column of Figure 3, the May-2012 snow depth was estimated from GPR using a
652 fixed radar velocity 0.25 m/ns along the lines within the plots, and then interpolated with a
653 simple linear interpolation in between the lines. The high-resolution GPR snow depth estimates
654 are useful for determining if microtopographic features can influence the distribution of snow
655 depths across each study plot. The high-resolution snow estimates over the large area allow us to
656 visually identify the macrotopographic control on snow depth. In Plot C, for example, the snow
657 depth does not have an increasing or decreasing trend, even though the elevation gradually
658 decreases towards east. Plot D, on the other hand, has more snow accumulation in the eastern
659 part of the domain, which is in the depression associated with DTLB.

660 PhoDAR-based Snow Depth Measurements

661 In the region of the 500-meter transects, the PhoDAR-derived snow-free DSMs (Figure 4a)
662 collected in July 2013 and August 2014 were first compared with the RTK DGPS data (acquired
663 in 2011) in Table 2, using the different schemes to identify co-location. We included the results
664 of both years to confirm the consistency between the two snow-free DSM products at the same
665 terrain. Although all the scheme yielded an excellent accuracy (the RMSE less than 7.0 cm),
666 taking the average provides the lowest RMSE in both years (6.41 cm in 2013 and 6.19 cm in
667 2014), which is approximately the same as the LiDAR data (RMSE = 6.08 cm). The PhoDAR-

Comment [Office8]: Comment R2-(1)

Deleted: The GPR estimates clearly reveal the influence of microtopography on snow depth at the resolution of a single-polygon scale and over the entire plot

Deleted: UAS

Deleted: d

Deleted: UAS

Comment [Office9]: Comment R2-(1)

Deleted: as

Deleted:

Deleted: Taking

Deleted: in the vicinity of each probe measurement

Deleted: RMSE =

Deleted: 0

Deleted: UAS

682 derived snow depth estimates in May 2015 were obtained by differencing the snow surface and
683 snow-free DSM (Figure 4b). The comparison between the PhoDAR-based snow estimates and
684 the snow depth probe data are favorable (Figure 4c), with a RMSE of 6.0 cm. When we removed
685 the points that had a large submeter-scale topographic variability in the vicinity (in the same way
686 and the same cut-off values as the GPR snow depth analysis), the RMSE improved to 4.6 cm
687 (Figure 4c).

Deleted: UAS

688

689 The PhoDAR-derived snow depth (Figure 4b) around the 500-meter transects in May 2015
690 reveals a similar pattern of snow distribution as the GPR data in Figure 3, having deeper snow in
691 the troughs and the centers of low-centered polygons. The high-resolution image of the PhoDAR,
692 data reveals more detail of the microtopographic effect than the interpolated image of the GPR
693 data, particularly in the narrow troughs. The large aerial coverage also shows the minimal effect
694 of macrotopography: while the elevation decreases towards south, the snow depth does not have
695 a large-scale trend.

Comment [Office10]: Comment R2-(1)

Deleted: UAS

Deleted: UAS

Deleted: in Figure 3

696

697 4.2. Snow Depth Variability over Tundra

698 *Variability among Different Polygon Types*

699 Figure 5 shows the boxplots of the snow depth, elevation, and microtopographic elevation
700 (Δ elevation) in each plot measured in May 2012. We used the coarse-grid snow depth probe
701 measurements, since the samples are uniformly distributed over each plot. The median snow
702 depth (Figure 5a) is fairly similar among four plots, even though they have different
703 geomorphologic features and polygon types. Tukey's pairwise comparison test (Table 3) shows
704 that only Plot B (small high-centered polygons) is significantly different from the other plots.

Comment [Office11]: Comment R2-(1)

709

710 The absolute elevation distribution varies among the four plots (Figure 5b), although the snow
711 depth for each of the plots has similar median values and distributions. Plot A (well-defined low-
712 centered polygons), for example, is at a higher elevation than Plots C (flat-centered polygons)
713 and D (low-centered polygons in DTLB), but the difference in the average snow depth is not
714 statistically significant (Table 3). The microtopographic elevation is computed based on the

715 wavelet transform with the scale of 32 m as described in Section 3.3 (Figure 5b). The scale of 32
716 m was selected to yield the best correlation between snow depth and microtopographic elevation.

Deleted: , removing the difference in the macrotopographic elevation among the four plots

717 Plot D (low-centered polygons in DTLB), for example, has less variability in both elevation and
718 snow depth, because Plot D has less distinct microtopography than others. In contrast, Plot B has
719 the largest variability in both microtopography and snow depth

Deleted: . In contrast, Plot B has large variability in both microtopography and snow depth

720

721 *Correlations between Snow Depth and Topographic Indices* in May 2012

Comment [Office12]: Comment R2-(1)

722 Among the topographic indices of macro- and microtopography, the snow depth in May 2012
723 (measured by the snow depth probe) was significantly correlated only to the microtopographic

Comment [Office13]: Comment R2-(1)

724 elevation for all plots (Figure 6a). The correlation coefficient changes with the scale of the
725 wavelet transform that separates micro- and macrotopography. The correlation coefficient is up
726 to -0.8 at Plot B (small high-centered polygons), and up to -0.7 at all the data points. The
727 correlation coefficient is different among different plots (i.e., different polygon types); the
728 correlation is less significant at Plot D (low-centered polygons in DTLB), than other plots. The
729 best correlation (i.e., the largest absolute value) can be achieved at a different scale in each plot
730 (Plot B < Plot A and Plot C < Plot D).

731

736 A significant correlation between snow depth and wind factor of macrotopography was identified
737 only in Plot D (low-centered polygons in DTLB; Figure 6b). The correlation coefficient is up to
738 0.41 at the scale of 38 m. Other topographic indices (i.e., the slope and curvature of both micro-
739 and macrotopography, the wind factor of microtopography) are not shown here, since we did not
740 find any significant correlation. Although Dvornikov et al. (2015) reported a strong correlation
741 between snow depth and curvature (snow free DEM), we did not find any significant correlation
742 in our data. This is possibly because the microtopography at our site was completely filled by
743 snow, and the overall elevation gradient at our site (the elevation difference in the domain is 3.1
744 m) is much smaller than the one that Dvornikov et al. (2015) reported (the elevation difference in
745 their domain was more than 60 m).

746

747 *Geostatistical Analysis of Snow Depth*

748 Spatial correlation exists for all three variables in May 2012: snow depth, snow surface, and
749 residual snow depth after removing the correlation to the microtopographic elevation (Table 4).

750 The correlation range is less than 20 m for the snow depth, which is consistent with the large
751 variability in a short distance. The snow surface, on the other hand, has a larger correlation range

752 (253 m). The estimation of a snow surface height (elevation + snow depth), effectively removes
753 the influence of microtopography, resulting in much a larger correlation range. The variance is

754 comparable between the snow depth and snow surface, while the variance is much lower in the
755 residual snow depth, since the topographic correlation explains a large portion of the snow depth
756 variability.

757

758 **4.3. Snow Depth Estimation based on LiDAR DEM**

Comment [Office14]: Comment R2-(1)

Deleted: Such a large correlation length is consistent with the field observation that the snow surface is smooth across the site.

762 Based on the snow-topography analysis in Section 4.2, we included the linear correlation
763 between snow and microtopographic elevation in Equation (1)₂ to describe the snow variability
764 in May 2012. We used the Shapiro-Wilk normality test to confirm that the residual of the linear
765 correlation, defined by τ in Equation (1), follows a normal distribution (the p-value of rejecting
766 this hypothesis was 0.21). The first column of the design matrix A is the microtopographic
767 elevation at all the pixels, and the second one is a vector of all ones. The parameter vector a is a
768 2-by-1 vector with the linear correlation parameters (slope and intercept). The Bayesian method
769 (Section 3.4) yielded 10,000 equally likely fields of the snow depth from the posterior
770 distribution in Equation (5).

771
772 The Bayesian estimated mean snow-depth field over the full study domain in May 2012 (Figure
773 7a) captures the effects of microtopography, such as more snow accumulation in polygon troughs
774 and centers of low-centered polygons. The snow depth does not have any large-scale trends over
775 the full study domain, which is different from the LiDAR DEM in Figure 1b, but consistent with
776 the interpolated GPR snow depths depicted in Figure 3 (right column), and the measured UAS
777 snow depth measurements depicted in Figure 4b. The variability is larger in the southern region
778 where there are high-centered polygons with deep troughs.

779
780 In addition, we compared this result (Figure 7a) with the mean field by estimating the snow
781 surface elevation and subtracting the ground surface elevation (Figure 7b). In this estimation, we
782 used the same Bayesian algorithm one described in Section 3.4, except that we removed the
783 topographic correlations and assumed a standard geostatistical model for snow surface (Diggle
784 and Ribeiro, 2007). In other words, we had the same algorithm except that we modified Equation

Comment [Office15]: Comment R2-(1)

Formatted: Font:Symbol, Bold

Comment [Office16]: Comment R2-(1)

Deleted: The estimated mean snow-depth field over the entire study region

Deleted: The snow depth does not have a large-scale trend over the domain, which is different from the LiDAR DEM in Figure 1, but consistent with the ground-based measurements (Figure 3 and 4)

Deleted: based on

Deleted: the kriging-based interpolation

Deleted: of

Deleted: (Diggle and Ribeiro, 2007)

795 (1) to $y = -z + x$, where $y + z$ represents the surface elevation. Although the two mean fields
796 (Figure 7) are similar in the central regions that have many measurements, the regions without
797 any measures have a significant deviation. This is because the snow surface estimation did not
798 capture the change in macrotopography (e.g. the drainage feature in the southern part of the
799 domain).

Formatted: Font:Bold, Italic
Deleted: T
Formatted: Font:Bold, Italic
Formatted: Font:Symbol, Bold, Italic
Formatted: Font:Bold, Italic
Deleted: , particularly

801 The estimated standard deviation of the Bayesian-derived snow depth over the study domain
802 (Figure 8a) also shows a significant difference from the one based on the snow surface
803 interpolation (Figure 8b). This standard deviation represents the uncertainty in the estimation. In
804 both cases, the standard deviation is smaller near the measurement locations along the transects
805 and within the four plots. However, when the topographic correlation is included (Figure 8a), the
806 standard deviation increases more rapidly as the pixel is farther away from the data points. This
807 is due to the fact that the spatial correlation range is small for the residual snow depth after
808 removing the topographic correlation (Table 4).

Deleted: .

Deleted: The estimated standard deviation of snow depth over the region
Deleted: , on the other hand,

810 Validation of the snow depth estimates over the study area (Plot A-D and the 500-meter
811 transects) was performed by comparing the estimates with the snow depth probe data (May
812 2012) not used in the procedure. The 100 points of the snow depth probe data were randomly
813 selected from all the locations (Plot A-D and the 500-meter transects), using a uniform
814 distribution. The validation results (Figure 9) show that the estimated confidence interval
815 captures the probe-measured snow depth. The estimated snow depth is distributed along with the
816 one-to-one line without any significant bias. The estimation, including the topographic
817 correlation (Figure 9a), has a tighter confidence interval and better estimation results than the

Comment [Office17]: Comment R2-(1)

Comment [Office18]: Comment R2-(1)
Deleted: (randomly selected)

Deleted:

826 one from interpolating the snow surface (Figure 9b). The RMSE for the Bayesian method of
827 estimating snow depth including the topographic correlation is 6.0 cm, while the RMSE for the
828 interpolated snow surface is 8.8 cm.

829

830

Deleted: The RMSE for including the topographic correlations is 6.0 cm, while the one for interpolating the snow surface is 8.8 cm

834 **5. Discussion**

835 **5.1. Different Observational Platforms**

836 Our analysis showed that GPR data provided the end-of-winter snow depth distribution with high
837 accuracy (RMSE = 2.9 cm) and resolution (10 cm along each line). The GPR-based estimation
838 requires care, particularly regarding the estimation of radar velocity and associated possible
839 errors, such as those due to positioning. Although the radar velocity is known to depend on the
840 snow density, we attribute the variability of radar velocity at our site to random or positioning
841 errors. Three results support this claim. First, the variability of radar velocity is smaller in a
842 thicker snow pack, suggesting the small contribution of the error relative to the overall snow
843 depth. The relatively low topographic variability over the site (compared to mountainous
844 terrains) would have contributed to this fairly uniform radar velocity. Second, the radar velocity
845 variability depends on the submeter-scale variability of the topography in the vicinity of the
846 calibration points, suggesting the impact of positioning errors. Third, there was no systematic
847 trend in the radar velocity as a function of the snow depth or topographic positions. We
848 developed a simple methodology (described in Section 3.1) to select co-located calibration points
849 based on the submeter-scale variability of topography, which proved to be useful to compute
850 accurate velocity. We note that – even though the depth-averaged radar velocity and hence the
851 depth-averaged snow density have little variability over the space –the snow density could be
852 variable vertically along the depth; we indeed found some layers of ice created by winter rain
853 events in the middle of the snow pack. It is possible that there might be a difference in the depth-
854 averaged density and radar velocity at a later time, when the snow pack starts to melt in a
855 heterogeneous manner.
856

857 UAS-based PhoDAR provided an attractive alternative for estimating snow depth at high
858 resolution over a large area. With much less labor and time, UAS-based PhoDAR can provide
859 many more sample points than GPR. The PhoDAR-based snow depth, however, was less
860 accurate than ground-based GPR or snow depth probe measurements (RMSE = 6.0 cm). The
861 main contribution of this error resulted from the snow-free elevation, since RMSE for the surface
862 DSM is around 6 cm. We note that the RMSE of 6.0 cm is still significantly more accurate than
863 the previous LiDAR and other airborne surveys (e.g., Deems et al., 2013; Harpold et al. 2014;
864 Nolan et al., 2015).

865

866 The PhoDAR-based approach is expected to continue its trajectory of continuous improvements
867 in terms of technical aspects, ease of use, and accuracy. At the time of our campaign, we were
868 allowed to use only a kite due to regulations, which led to a limited number of pictures that could
869 be used to reconstruct the DSM. The accuracy will significantly improve with the use of a light
870 unmanned aerial vehicle (UAV). Although UAS-based LiDAR acquisition technology continues
871 to improve (e.g., Anderson and Gaston, 2013), and is expected to be a powerful alternative to
872 characterize snow, the LiDAR device is still significantly more expensive than a conventional
873 camera (roughly by factor of 100). Given that the vegetation height is fairly small in the Arctic
874 tundra, the PhoDAR technique is an affordable alternative,

875

876 For all the types of measurements, accurate positioning was critical in the polygonal tundra due
877 to microtopography. The GPS snow depth probe (Snow-Hydro), for example, had the positioning
878 error larger than 50 cm, and required extra post-processing to correct the locations. On the other
879 hand, measuring the RTK DGPS at all the snow depth measurement locations would not be

Deleted: UAS

Deleted: point

Deleted: UAS

Deleted: n

Deleted: option

885 realistic since it would take time. We found that having a measurement tape and measuring the
886 start and end points by the DGPS were a reasonable approach, when the snow surface is smooth
887 and hard. In this study, we used the snow depth probe data as the true snow depth to compare
888 with other measurements (i.e., GPR, PhoDAR, and Bayesian estimation). To improve the
889 accuracy further, it would be necessary to quantify the uncertainty in the snow depth probe
890 associated with the vegetation and other issues (Berezovskaya and Kane, 2007).

Deleted: measure

891

892 **5.2. Snow Depth Variability**

Deleted: .

893 The end-of-year snow depth distribution at the ice-wedge polygons was highly variable over a
894 short distance in May 2012. The snow depth was, however, significantly correlated with the
895 microtopographic elevation, suggesting that the snow depth could be described by
896 microtopography. The wind-blown snow transport leads to significant snow redistribution, and
897 fills microtopographic lows (i.e., troughs and centers of low-centered polygons) with thicker
898 snow pack (e.g., Pomeroy et al., 1993). The redistribution also results in the smooth snow
899 surface, following the macrotopography. The exception was observed at the edge of the DTLB,
900 where the abrupt change in macrotopography led to increased accumulation in the depression.
901 This is a similar effect to that observed along the riverbanks by Benson and Sturm (1993).
902 Although the tundra ecosystem studies have focused on the effect of microtopography (e.g.,
903 Zona et al., 2011), the macrotopography also may be important when we characterize snow
904 distribution over a larger area.

Comment [Office19]: Comment R2-(1)

905

906 The “average” snow depth over a hundred-meter scale (i.e., the size of Plot A-D), on the other
907 hand, was fairly uniform across the site despite the different polygon types in May 2012. Plot A

Comment [Office20]: Comment R2-(1)

910 (well-defined low-centered polygons) and C (flat-centered polygons), for example, have different
911 polygon types, but they have a similar average snow depth. This is because microtopography and
912 microtopographic features (i.e., polygon troughs, rims) mainly control the snow distribution. Plot
913 B (small high-centered polygons) is an exception, having smaller median snow depth than the
914 other plots. Plot B has the largest variability in microtopography, characterized by the small
915 round high-centered polygons, like numerous small mounds (Figure 3). Such mounds are prone
916 to erosion by the wind, and hence lead to less snow trapping and accumulation.

917

918 Identifying such correlations between snow depth and topography requires an effective approach
919 to separate micro- and macrotopography. Our wavelet analysis revealed that the separation scale
920 depends on the polygon sizes; for example, the larger polygons in Plot A (well-defined low-
921 centered polygons) and C (flat-centered polygons) lead to a larger separation scale than the
922 smaller polygons in Plot B (small high-centered polygons). It is a challenge to map
923 macrotopography accurately over a larger area, particularly at the present site, where different
924 types and sizes of polygons mix. Although we used the same scale for the estimation, an,
925 improved polygon delineation algorithm will possibly enable us to separate micro- and
926 macrotopography in the future (e.g., Wainwright et al., 2015).

927

928 **5.3. Snow Depth Estimation**

929 The developed Bayesian approach enabled us to estimate the snow depth distribution over a large
930 area based on the LiDAR DEM and the correlation between the snow depth and topography.

931 Although this paper only used the ground-based GPR and snow depth probe measurements
932 collected at the same time, PhoDAR could be easily included in the same framework. The

Deleted: the

Deleted: UAS

935 Bayesian method allowed us to integrate three types of datasets (LiDAR DEM, snow depth
936 probe and GPR) in a consistent manner, and also provided the uncertainty estimate for the
937 estimated snow depth. Taking into account the topographic correlation explicitly improved the
938 accuracy of estimation significantly (RMSE 6.0 cm), compared to interpolating the snow surface
939 and subtracting the DEM (RMSE 8.8 cm).

941 Our approach can be extended to snow estimates over both time and space. The correlations
942 between snow depth and topography may change over time. In early and later winter, for
943 example, the snow depth would be more affected by curvature and slope of microtopography,
944 since the microtopographic lows (troughs and centers of the low-centered polygons) are not
945 filled by snow. ~~It would be possible to quantify the seasonal changes in the topography-snow
946 correlations by designing a full season ground-based measurement campaign and acquisition of
947 remote sensing snow depth measurements (by PhoDAR or LiDAR), that monitored the same site
948 over several years to account for inter-annual variability.~~ The Bayesian method presented here is
949 flexible enough to account for changes in parameters over time for the spatial-temporal data
950 integration (e.g., Wikle et al., 2001). Although physically-based snow distribution models can be
951 used for the same purposes (e.g., Pomeroy et al., 1993; Liston and Sturm, 1998; 2002), it is
952 difficult to parameterize all the processes, such as sublimation and turbulent transport. Our data-
953 driven approach provides a powerful alternative to distribute snow depth based on various
954 datasets.

Formatted: Not Highlight

Deleted: It would be possible to quantify the changes in the topography-snow correlations by designing ground-based measurements and remote sensing snow surface measurements (by UAS)

959 **6. Summary**

960 In this study, we explored various strategies to estimate the end-of-year snow depth distribution

961 over an Arctic ice-wedge polygon tundra region. We first developed an effective methodology to

962 calibrate GPR and PhoDAR in the presence of submeter-scale-scale variability of topography.

963 We then investigated the characteristics and accuracy of three observational platforms: snow

964 depth, probe, GPR and PhoDAR. The PhoDAR-derived snow depth estimates have great

965 potential for accurately characterizing snow depth over larger regions (with an RMSE of 4.6 cm),

966 relative to the in situ snow depth measurements. The GPR snow depth estimates were slightly

967 more accurate (with an RMSE of 2.9 cm), but required considerable more effort to obtain, and

968 require complex post-processing to minimize errors associated with radar positioning.

969

970 We investigated the spatial variability of the snow depth and its dependency on the topographic

971 metrics. At the peak snow depth during our data acquisition, the snow depth was highly

972 correlated with microtopographic elevation (the correlation coefficient of up to -0.8), although it

973 was highly variable over short distances (the correlation range of 12.3 m). It is considered that

974 the wind redistribution filled the microtopography by snow, and created a snow surface,

975 following macrotopography at the site. The challenge was to separate macro- and

976 microtopography, since the separation scale was not arbitrary, and depended on the polygon size.

977 The wavelet analysis provided an effective approach to identify this separation scale.

978

979 The Bayesian method was effective at integrating different measurements to estimate snow depth

980 distribution over the site. Although our estimation is based on the data collected from a one-time

981 campaign, and the correlations to topography may change over time, the approach developed

Deleted:

Deleted: UAS

Deleted: complex

Deleted: microtopographic

Deleted: point

Deleted: UAS

Deleted: Although UAS showed a great potential for characterizing the snow depth over a large area, the ground-based observations were still more accurate.

Deleted: The

Deleted: created

Deleted: a smooth snow surface,

994 here is expected to be applicable for estimating both spatial and temporal variability of snow
995 depth at other sites, and in other landscapes.
996

Deleted: (prairie)extensible

Deleted: for estimating both spatial and temporal variability of snow depth and for exploring the influence of snow depth on ecosystem functioning

1001 **Appendix A**

1002 In MCMC, we sample each variable sequentially conditioned on all the other variables. In other
1003 words, when we update one variable (or one vector), we assume that the other variables are
1004 known and fixed. After sampling thousands of sets of the variables, the distribution of those
1005 samples converges to the posterior distribution. Each vector is sampled as follows:

1006

1007 The snow depth field is sampled from the distribution:

1008
$$p(\mathbf{y} | \bullet) = p(\mathbf{y} | \mathbf{a}, \mathbf{b}, \mathbf{z}_d, \mathbf{z}_g, \mathbf{z}_p) \propto p(\mathbf{z}_g | \mathbf{y}, \mathbf{b}) p(\mathbf{z}_p | \mathbf{y}) p(\mathbf{y} | \mathbf{a}, \mathbf{z}_d) \quad (\text{A.1})$$

1009 where “•” represents all the other variables. The distribution is decomposed to a series of small
1010 conditional distributions defined in Table 1. Similarly, we can sample the snow-process
1011 parameters \mathbf{a} and GPR-data parameter \mathbf{b} from the distributions:

1012
$$p(\mathbf{a} | \bullet) = p(\mathbf{a} | \mathbf{y}, \mathbf{h}) \propto p(\mathbf{y} | \mathbf{h}, \mathbf{a}) p(\mathbf{a}) \quad (\text{A.2})$$

1013
$$p(\mathbf{b} | \bullet) = p(\mathbf{b} | \mathbf{y}, \mathbf{z}_g) \propto p(\mathbf{z}_g | \mathbf{y}, \mathbf{b}) p(\mathbf{b}) \quad (\text{A.3})$$

1014 Since all the distributions in Equation A.1–A.3 are multivariate Gaussian, we can use the
1015 conjugate prior to compute an analytical form of each distribution. Each distribution is
1016 multivariate Gaussian with the covariance and mean vector defined in Table A.1. In the Gibbs’
1017 sampling algorithm, we sample each variable vector sequentially until the distributions are
1018 converged.

1019

1020 **Appendix B**

1021 The workflow of the Bayesian geostatistical approach from the data is included in Figure B.1.
1022 The snow depth probe data and LiDAR DEM are used to (a) identify the correlations between
1023 topography and snow depth (Section 3.3) after identifying the representative scale of macro- and

Formatted: Font:Bold

1024 micro-topography in the wavelet analysis, to (b) quantify the variogram parameters, and also to
1025 (c) create a process model in Equation (1). The GPR data are analyzed to estimate the radar
1026 velocity, and to quantify the correlations to the snow depth probe (Section 3.1). At the end (the
1027 last column in Figure B.1), all the parameters are assembled for the estimation using MCMC
1028 (Appendix A).

1029

1030

1031 **Acknowledgements**

1032 The Next-Generation Ecosystem Experiments (NGEE) Arctic project is supported by the Office
1033 of Biological and Environmental Research in the DOE Office of Science. This NGEE-Arctic
1034 research is supported through contract number DE-AC0205CH11231 to Lawrence Berkeley
1035 National Laboratory. We gratefully acknowledge Stan Wullschleger in Oak Ridge National
1036 Laboratory, project PI. We thank Dr. Craig Tweedie at University of Texas, El Paso for
1037 providing the LiDAR dataset, and together with Sergio Vargas from University of Texas, El
1038 Paso, for providing kite-based landscape imaging advice. Datasets are available upon request by
1039 contacting the corresponding author (Haruko M. Wainwright, hmwainwright@lbl.gov).
1040

Formatted: Tabs:Not at 0.2" + 3.2" + 6.5"

Deleted:)

Deleted: .

1043 **Reference:**

- 1044 Anderson, B. T., McNamara, J. P., Marshall, H. P., & Flores, A. N. (2014). Insights into the
1045 physical processes controlling correlations between snow distribution and terrain properties.
1046 Water Resources Research, 50(6), 4545-4563.
- 1047 Anderson, K., and Gaston, K. J. (2013). Lightweight unmanned aerial vehicles will revolutionize
1048 spatial ecology. *Frontiers in Ecology and the Environment*, 11(3), 138-146.
- 1049 [Annan, A.P., 2005, Ground penetrating radar, in near surface geophysics, in D.K. Butler \(eds\),](#)
1050 [Society of Exploration Geophysicists, Tulsa, OK, USA, Investigations in Geophysics No. 13,](#)
1051 [pp. 357-438.](#)
- 1052 Benson, C. S., and Sturm, M. (1993). Structure and wind transport of seasonal snow on the
1053 Arctic slope of Alaska. *Annals of Glaciology*, 18, 261-267.
- 1054 [Berezovskaya S, Kane DL. 2007. Measuring snow water equivalent for hydrological](#)
1055 [applications: part 1, accuracy of observations. In: Proceedings of the 16th International](#)
1056 [Northern Research Basins Symposium and Workshop. Petrozavodsk, Russia](#)
1057 http://resources.krc.karelia.ru/krc/doc/publ2007/SYMPOSIUM_029-35.pdf
- 1058 Binley, A., Hubbard, S.S., Huisman, J., Revil, A., Robinson, D., Singha, K., and Slater, L. (2015)
1059 The emergence of hydrogeophysics for improved understanding of subsurface processes over
1060 multiple scales. DOI: 10.1002/20015WR017016
- 1061 Bowling, L. C., D. L. Kane, R. E. Gieck, L. D. Hinzman, and D. P. Lettenmaier, The role of
1062 surface storage in a low-gradient Arctic watershed, *Water Resour. Res.*, 39(4), 1087,
1063 doi:10.1029/2002WR001466, 2003.
- 1064 Bjørke, J. T., and Nilsen, S. (2003). Wavelets applied to simplification of digital terrain models.
1065 *International Journal of Geographical Information Science*, 17(7), 601-621.

1066 Brown, J. (1967), Tundra soils formed over ice wedges, northern Alaska, *Soil Sci. Soc. Am. J.*,
1067 31(5), 686–691

1068 Callaghan, T. V., M. Johansson, R.D. Brown, P. Y. Groisman, N. Labba, V. Radionov, R.S.
1069 Bradley, S. Blangy, O.N. Bulygina, T.R. Christensen, J.E. Colman, R.L.H. Essery, B.C.
1070 Forbes, M.C. Forchhammer, V.N. Golubev, R. E. Honrath, G.P. Juday, A.V. Meshcherskaya,
1071 G.K. Phoenix, J. Pomeroy, A. Rautio, D.A. Robinson, N.M. Schmidt, M.C. Serreze, V.P.
1072 Shevchenko, A.I. Shiklomanov, A.B. Shmakin, P. Sköld, M. Sturm, M. Woo, E. F. Wood,
1073 (2011). Multiple Effects of Changes in Arctic Snow Cover. *Ambio*, 40 (Suppl 1), 32–45.
1074 Doi:10.1007/s13280-011-0213-x

1075 Clein, J. S., & Schimel, J. P. (1995). Microbial activity of tundra and taiga soils at sub-zero
1076 temperatures. *Soil Biology and Biochemistry*, 27(9), 1231-1234.

1077 [Dafflon, B., Hubbard, S., Ulrich, C., Peterson, J., Wu, Y., Wainwright, H., & Kneafsey, T. J.](#)
1078 [\(2016\). Geophysical estimation of shallow permafrost distribution and properties in an ice-](#)
1079 [wedge polygon-dominated Arctic tundra region. *Geophysics*, 81\(1\), WA247-WA263.](#)

1080 Davison, A. C. (2003). *Statistical models* (Vol. 11). Cambridge University Press.

1081 Deems, J. S., Painter, T. H., & Finnegan, D. C. (2013). Lidar measurement of snow depth: a
1082 review. *Journal of Glaciology*, 59(215), 467-479.

1083 [Day-Lewis, F. D., and J. W. Lane Jr. \(2004\), Assessing the resolution-dependent utility of](#)
1084 [tomograms for geostatistics, *Geophys. Res. Lett.*, 31, L07503, doi:10.1029/2004GL019617.](#)

1085 [Derksen, C., A. Silis, M. Sturm, J. Holmgren, G. Liston, H. Huntington, and D. Solie, 2009:](#)
1086 [Northwest Territories and Nunavut Snow Characteristics from a Subarctic Traverse:](#)
1087 [Implications for Passive Microwave Remote Sensing. *J. Hydrometeor.*, 10, 448–463, doi:](#)
1088 [10.1175/2008JHM1074.1.](#)

1089 [Diggle, P. and Ribeiro, P. J. \(2007\). Model-based geostatistics. Springer Science & Business](#)
1090 [Media.](#)

1091 Dvornikov, Y., Khomutov, Mullanurov, and Ermokhina (2015), GIS- and field data based
1092 modeling of snow water equivalent in shrub tundra, Ice and Snow, doi:10.15356/2076-6734-
1093 2015-2-69-80.

1094 [Engstrom, R., Hope, A., Kwon, H., Stow, D., & Zamolodchikov, D. \(2005\). Spatial distribution](#)
1095 [of near surface soil moisture and its relationship to microtopography in the Alaskan Arctic](#)
1096 [coastal plain. Hydrology Research, 36\(3\), 219-234.](#)

1097 Gamerman, D. and H. F. Lopes (2006), Markov Chain Monte Carlo – Stochastic simulation for
1098 Bayesian inference. Chapman&Hall/CRC, 2nd edition, Boca Raton, USA.

1099 Gamon, J. A., G. P. Kershaw, S. Williamson, and D. S. Hik (2012), Microtopographic patterns in
1100 an arctic baydjarakh field: do fine-grain patterns enforce landscape stability? Environ. Res.
1101 Lett., 7(1), 015502.

1102 Geweke, J. (1992), Evaluating the accuracy of sampling-based approaches to calculating
1103 posterior moments, in Bayesian Statistics 4 (edited by J. M. Bernardo, J. O. Berger, A. P.
1104 Dawid and A. F. M. Smith), Clarendon Press, Oxford, UK.

1105 [Gillin, C., S. Bailey, K. McGuire, and J. Gannon \(2015\), Mapping of Hydropedologic Spatial](#)
1106 [Patterns in a Steep Headwater Catchment, Soil Science Society of America Journal, 79\(2\),](#)
1107 [440, doi:10.2136/sssaj2014.05.0189.](#)

1108 Gusmeroli, A., and Grosse, G. (2012). Ground penetrating radar detection of subsnow slush on
1109 ice-covered lakes in interior Alaska. The Cryosphere, 6(6), 1435-1443.

Deleted: -

Deleted: -

Formatted: Superscript

1112 Gusmeroli, A., G. Wolken, and A. Arendt (2014), Helicopter-borne radar imaging of snow cover
1113 on and around glaciers in Alaska, *Annals of Glaciology*, 55(67), 78–88,
1114 doi:10.3189/2014aog67a029.

1115 Harper, JT, and JH Bradford (2003), Snow stratigraphy over a uniform depositional surface:
1116 spatial variability and measurement tools, *Cold Regions Science and Technology*.

1117 Harpold, A. A., et al. (2014), LiDAR-derived snowpack data sets from mixed conifer forests
1118 across the Western United States, *Water Resour. Res.*, 50, doi:10.1002/2013WR013935.

1119 Hinkel, K. M., W. R. Eisner, J. G. Bockheim, F. E. Nelson, K. M. Peterson, and X. Dai (2003),
1120 Spatial extent, age, and carbon stocks in drained thaw lake basins on the Barrow Peninsula,
1121 Alaska, *Arct., Antarct., and Alp. Res.*, 35(3), 291-300.

1122 [Hirashima, H., Y. Kodama, N. Sato, T. Ohata, H. Yabuki, and A. Georgiadi, 2004: Nonuniform](#)
1123 [Distribution of Tundra Snow Cover in Eastern Siberia. *J. Hydrometeor.*, 5, 373–389, doi:](#)
1124 [10.1175/1525-7541\(2004\)005<0373:NDOTSC>2.0.CO;2.](#)

1125 Hubbard, S. and Y. Rubin (2005), Hydrogeophysics, Chapter 1 in *Hydrogeophysics*, Eds. Y.
1126 Rubin and S. Hubbard, Elsevier.

1127 Hubbard, S. S., C. Gangogadagamage, B. Dafflon, H. Wainwright, J. E. Peterson, A. Gusmeroli, C.
1128 Ulrich, Y. Wu, C. Wilson, C., J. Rowland, C. Tweedie, and S. D. Wulschleger (2013),
1129 Quantifying and relating land-surface and subsurface variability in permafrost environments
1130 using LiDAR and surface geophysical datasets, *Hydrogeol. J.*, 21(1), 149-169.

1131 Jansson, JK, and N Taş (2014), The microbial ecology of permafrost, *Nature Reviews*
1132 *Microbiology*, doi:10.1038/nrmicro3262.

1133 [Jol., H.M., \(2009\), *Ground Penetrating Radar Theory and Applications*, Elsevier Science.](#)

- 1134 Kane, D. L., L. D. Hinzman, C. S. Benson, and G. E. Liston (1991), Snow hydrology of a
1135 headwater Arctic basin: 1. Physical measurements and process studies, *Water Resour. Res.*,
1136 27(6), 1099–1109, doi:10.1029/91WR00262.
- 1137 Kalbermatten, M. (2010). Multiscale analysis of high resolution digital elevation models using
1138 the wavelet transform, Thesis, Ecole Polytechnique Federale de Lausanne.
- 1139 Kalbermatten, M., Van De Ville, D., Turberg, P., Tuia, D., & Joost, S. (2012). Multiscale
1140 analysis of geomorphological and geological features in high resolution digital elevation
1141 models using the wavelet transform. *Geomorphology*, 138(1), 352-363.
- 1142 [Leffingwell, E. D. K. \(1915\). Ground-ice wedges: The dominant form of ground-ice on the north](#)
1143 [coast of Alaska, *J. Geol.*, 635-654.](#)
- 1144 Liljedahl, A. K., Hinzman, L. D., Harazono, Y., Zona, D., Tweedie, C. E., Hollister, R. D.,
1145 Engstrom, R., and Oechel, W. C. (2011) Nonlinear controls on evapotranspiration in arctic
1146 coastal wetlands, *Biogeosciences*, 8, 3375-3389, doi:10.5194/bg-8-3375-2011.
- 1147 Liljedahl, A. K., Boike, J., Daanen, R. P., Fedorov, A. N., Frost, G. V., Grosse, G., ~~...~~ &
1148 Necsoiu, M. (2016). Pan-Arctic ice-wedge degradation in warming permafrost and its
1149 influence on tundra hydrology. *Nature Geoscience*.
- 1150 Liston, G. E., and Sturm, M. (1998). A snow-transport model for complex terrain. *Journal of*
1151 *Glaciology*, 44(148), 498-516.
- 1152 Liston, G., and Sturm, M. (2002). Winter precipitation patterns in arctic Alaska determined from
1153 a blowing-snow model and snow-depth observations. *Journal of Hydrometeorology*, 3, 646–
1154 659.
- 1155 MacKay, J. R. (2000), Thermally induced movements in ice-wedge polygons, western Arctic
1156 coast: a long-term study, *Géographie physique et Quaternaire*, 54(1), 41-68.

Deleted: ...

1158 Machguth, H, O. Eisen, F. Paul, and M Hoelzle (2006), Strong spatial variability of snow
1159 accumulation observed with helicopter borne GPR on two adjacent Alpine glaciers,
1160 Geophysical Research Letters, 33(13), doi:10.1029/2006GL026576.

1161 [Murakami, H., Chen, X., Hahn, M. S., Liu, Y., Rockhold, M. L., Vermeul, V. R., Zachara, J. M.,
1162 and Rubin, Y. \(2010\), Bayesian approach for three-dimensional aquifer characterization at the
1163 Hanford 300 Area, *Hydrol. Earth Syst. Sci.*, 14, 1989-2001, doi:10.5194/hess-14-1989-2010.](#)

1164 Nobrega, S, and P Grogan (2007), Deeper snow enhances winter respiration from both plant-
1165 associated and bulk soil carbon pools in birch hummock tundra, *Ecosystems*,
1166 doi:10.1007/s10021-007-9033-z.

1167 Nolan, M., C. Larsen, and M. Sturm (2015), Mapping snow depth from manned aircraft on
1168 landscape scales at centimeter resolution using structure-from-motion photogrammetry,
1169 *Cryosphere*, 9(4), 1445–1463, doi:10.5194/tc-9-1445-2015.

1170 Osterkamp, T. E. (2007), Causes of warming and thawing permafrost in Alaska, *Eos Trans.*
1171 *AGU*, 88(48), 522–523, doi:10.1029/2007EO480002.

1172 Pomeroy, J.W., Gray, D.M. and Landine, P.G., 1993. The Prairie Blowing Snow Model:
1173 characteristics, validation, operation. *J. Hydrol.*, 144: 165-192.

1174 [Pomeroy, J. W., Marsh, P. and Gray, D. M. \(1997\), Application of a distributed blowing snow
1175 model to the Arctic. *Hydrol. Process.*, 11: 1451–1464. doi:10.1002/\(SICI\)1099-
1176 1085\(199709\)11:11<1451::AID-HYP449>3.0.CO;2-Q](#)

1177 [Proksch, M., Löwe, H. and Schneebeli, M. \(2015\), Density, specific surface area, and correlation
1178 length of snow measured by high-resolution penetrometry. *J. Geophys. Res. Earth Surf.*, 120:
1179 346–362. doi: 10.1002/2014JF003266.](#)

1180 [Rees, A., English, M., Derksen, C., Toose, P. and Silis, A. \(2014\), Observations of late winter](#)
1181 [Canadian tundra snow cover properties. *Hydrol. Process.*, 28: 3962–3977.](#)
1182 [doi:10.1002/hyp.9931](#)

1183 [Ribeiro, P.J., Diggle, P.J. \(2001\). *geoR: a package for geostatistical analysis*. 15-18. ISSN R-](#)
1184 [NEWS 1 \(2\), 1609–3631.](#)

1185 Smith, M.J., J. Chandler, and J. Rose (2009), High spatial resolution data acquisition for the
1186 geosciences: kite aerial photography, *Earth Surf. Proc. and Land.*, 34(1), 155-161.

1187 Stieglitz, M., S.J. De 'ry, V. E. Romanovsky, and T. E. Osterkamp, The role of snow cover in the
1188 warming of arctic permafrost, *Geophys. Res. Lett.*, 30(13), 1721,
1189 [doi:10.1029/2003GL017337](#), 2003.

1190 [Sturm, M., and A. M. Wagner \(2010\), Using repeated patterns in snow distribution modeling: An](#)
1191 [Arctic example, *Water Resour. Res.*, 46, W12549, doi:10.1029/2010WR009434.](#)

1192 Schimel, J. P., Bilbrough, C., & Welker, J. M. (2004). Increased snow depth affects microbial
1193 activity and nitrogen mineralization in two Arctic tundra communities. *Soil Biology and*
1194 *Biochemistry*, 36(2), 217-227.

1195 Sjögersten, S., van der Wal, R., and Woodin, S. J. (2006). Small-scale hydrological variation
1196 determines landscape CO₂ fluxes in the high Arctic. *Biogeochemistry*, 80(3), 205–216.
1197 [doi:10.1007/s10533-006-9018-6.](#)

1198 Sturm, M., Schimel, J., Michaelson, G., Welker, J. M., Oberbauer, S. F., Liston, Fahnestock J.
1199 and Romanovsky, V. E. (2005). Winter biological processes could help convert arctic tundra
1200 to shrubland. *Bioscience*, 55(1), 17-26.

1201 Tiuri, M. E., A. H. Sihvola, E. G. Nyfors, and M. T. Hallikaiken (1984), The complex dielectric
1202 constant of snow at microwave frequencies, *Oceanic Engineering, IEEE Journal of*, 9(5),
1203 377–382, doi:10.1109/JOE.1984.1145645.

1204 Wainwright, H. M., J. Chen, D. S. Sassen, and S. S. Hubbard (2014), Bayesian hierarchical
1205 approach and geophysical data sets for estimation of reactive facies over plume scales, *Water*
1206 *Resour. Res.*, 50, 4564–4584, doi:10.1002/2013WR013842.

1207 Wainwright, H. M., B. Dafflon, L. J. Smith, M. S. Ha hn, J. B. Curtis, Y. Wu, C. Ulrich, J.E.
1208 Peterson, M.S. Torn, and S.S. Hubbard (2015), Identifying multi scale zonation and assessing
1209 the relative importance of polygon geomorphology on carbon fluxes in an Arctic tundra
1210 ecosystem, *J. Geophys. Res. Biogeosci.*, 120,788–808, doi:10.1002/2014JG002799.

1211 Wainwright, H. M., A. Flores Orozco, M. Bücken, B. Dafflon, J. Chen, S. S. Hubbard, and K. H.
1212 Williams (2016), Hierarchical Bayesian method for mapping biogeochemical hot spots using
1213 induced polarization imaging, *Water Resour. Res.*, 52, doi:10.1002/2015WR017763.

1214 Wikle, C. K., R. F. Milliff, D. Nychka, and L. M. Berliner (2001), Spatiotemporal hierarchical
1215 Bayesian modeling: Tropical ocean surface winds, *J. Am. Stat. Assoc.*, 96(454), 382–397.

1216 Zhang, T. J. (2005). Influence of the seasonal snow cover on the ground thermal regime: An
1217 overview. *Reviews of Geophysics* 43: RG4002. doi:10.1029/2004RG000157.

1218 Zona, D., D. A. Lipson, R. C. Zulueta, S. F. Oberbauer, and W. C. Oechel (2011),
1219 Microtopographic controls on ecosystem functioning in the Arctic Coastal Plain, *J. Geophys.*
1220 *Res. Biogeo.* (2005–2012), 116(G4).

1221 Zona, D., Gioli, B., Commane, R., Lindaas, J., Wofsy, S. C., Miller, C. E., ... & Chang, R. Y. W.
1222 (2016). Cold season emissions dominate the Arctic tundra methane budget. *Proceedings of the*
1223 *National Academy of Sciences*, 113(1), 40-45.

1224 **List of Figures**

1225 Figure 1. (a) Location of Barrow, Alaska, USA, and Barrow Environmental Observatory (BEO)
1226 from Hubbard et al. (2013). (b) NGEE-Arctic site with the digital elevation map from the
1227 airborne LiDAR (in meters). The black boxes are the intensive sampling plots (Plot A, B, C and
1228 D). The white rectangles are the fine-grid snow depth measurements by a snow depth probe. The
1229 three black lines represent the 500-meter transects.

1230
1231 Figure 2. Radar velocity as a function of (a) co-located snow depth measured by a snow depth
1232 probe and (b) elevation difference (i.e., topographic variability) within 1 m. (c) Comparison
1233 between the probe-derived and GPR-derived snow depth at all the co-located locations (blue
1234 circles) and at selected locations (red circles) where topographic variability is low. In (a), the
1235 black vertical line is the median snow depth, and the dotted lines are +/- one STDEV from the
1236 median snow depth. In (b), the black line is the cut-off elevation difference of 0.05 m.

1237
1238 Figure 3. Elevation and snow depth in Plots A, B, C and D. The left column is LiDAR DEM (in
1239 meters), the middle column is the probe measured snow depth (in meters), and the right column
1240 is the interpolated snow depth estimated using GPR (in meters).

1241
1242 Figure 4. (a) PhoDAR-derived DSM in meters (August, 2014), (b) PhoDAR-derived snow depth
1243 in meters (May, 2015), and (c) comparison between the PhoDAR-based and probe-based snow
1244 depth at all the locations (blue circles) and at selected locations (red circles) having low
1245 topographic variability (the sub-meter elevation variability less than 0.05 m). The black line in
1246 (b) represents the snow depth probe measurements every 3 meter along the 500-meter transect.

Deleted: Figure 1. (a) Location of Barrow, Alaska, USA, and Barrow Environmental Observatory (BEO) from Hubbard et al. (2013). (b) NGEE-Arctic site with the digital elevation map from the airborne LiDAR (in meters). The black boxes are the intensive sampling plots (Plot A, B, C and D). The white rectangles are the fine-grid snow depth measurements by a point probe. The three black lines represent the transects. .
Deleted: point

Deleted: .

Deleted: Figure 4. (a) UAS-derived DSM in meters (August, 2014), (b) UAS-derived snow depth in meters (May, 2015), and (c) comparison between the UAS-based and probe-based snow depth at all the locations (blue circles) and at selected locations (red circles) having low topographic variability. .

1263 Figure 5. Boxplots of (a) snow depth and (b) elevation and (c) microtopographic elevation in
1264 Plots A-D.

1265

1266 Figure 6. Correlation coefficients between snow depth and topographic metrics as a function of
1267 the wavelet scale: (a) the microtopographic elevation, and (b) the wind factor of
1268 macrotopography. The different colors represent different plots (Plot A–D) or all the data (All).
1269 Each dash line represents the scale that maximize the magnitude of the correlation coefficient.

1270

1271 Figure 7. The estimated mean snow depth across the site (in meters) based on (a) the proposed
1272 Bayesian method including the correlation to microtopography, and (b) the kriging-based
1273 interpolation of the snow surface. The spatial extent is the same as Figure 1b.

1274

1275 Figure 8. The estimated standard deviation of snow depth across the site (in meters) based on (a)
1276 the proposed Bayesian method including the correlation to microtopography, and (b) the kriging-
1277 based interpolation of the snow surface. The spatial extent is the same as Figure 1b.

1278

1279 Figure 9. Estimated mean and confidence intervals from the Bayesian method, compared to the
1280 probe-measured snow depth by (a) using the correlation to microtopography and (b) interpolating
1281 the snow surface. The red circles represent the snow depth at the validation locations (the snow
1282 depth probe measurements not used in the estimation), the blue lines are the confidence intervals
1283 based on the standard deviation (STD) multiplied by 1.9 (94% confidence intervals), and the
1284 black lines are the one-to-one line.

1285

Deleted: Figure 6. Correlation coefficients between snow depth and topographic metrics as a function of the wavelet scale: (a) the microtopographic elevation, and (b) the wind factor of macrotopography. - ... [1]

1291 **List of Tables**

1292 Table 1. Multivariate normal distribution defined for each variable.

1293

1294 Table 2. Root mean squared error (RMSE) between the PhoDAR-derived DSM and GPS
1295 elevation measurements based on the three schemes: nearest neighbor, average, and minimum
1296 elevation within the 0.5 m radius.

Deleted: UAS

1297

1298 Table 3. p values from Tukey's pairwise comparison test for each pair of the plots.

1299

1300 Table 4. Estimated geostatistical parameters and covariance models for snow depth, snow
1301 surface and residual snow depth.

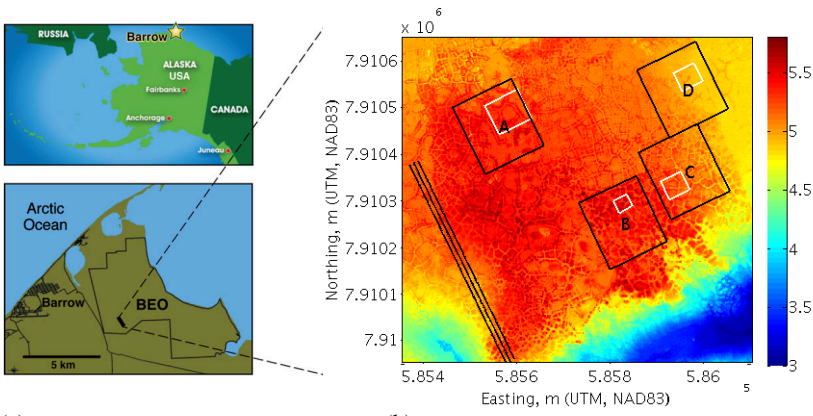
1302

1303 Table A.1. Posterior distributions during the Gibbs sampling.

Deleted: -

... [2]

1304



1308
 1309
 1310
 1311
 1312
 1313
 1314
 1315

(a) Location of Barrow, Alaska, USA, and Barrow Environmental Observatory (BEO) from Hubbard et al. (2013). (b) NGEE-Arctic site with the digital elevation map from the airborne LiDAR (in meters). The black boxes are the intensive sampling plots (Plot A, B, C and D). The white rectangles are the fine-grid snow depth measurements by a snow depth probe. The three black lines represent the 500-meter transects.

Deleted: point

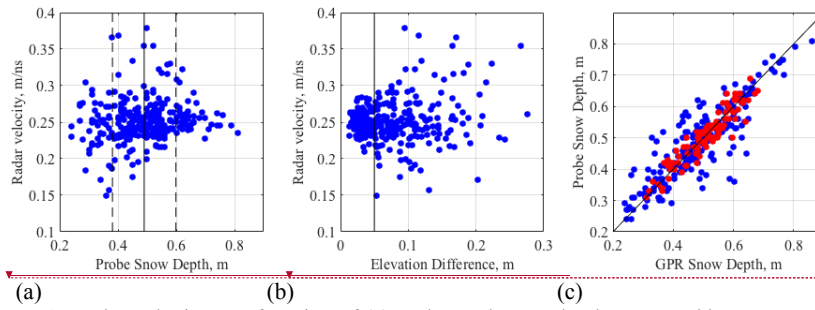
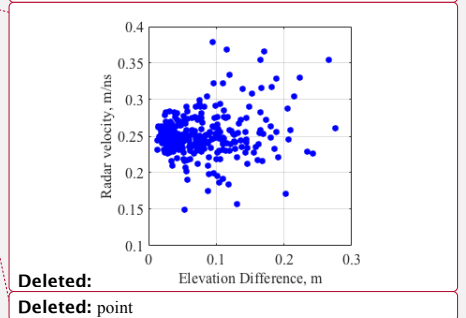
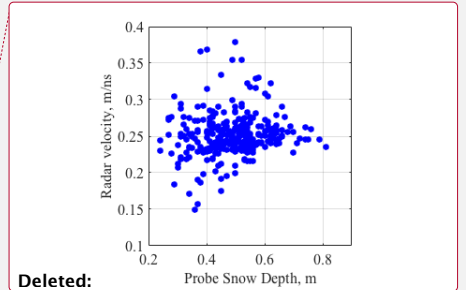
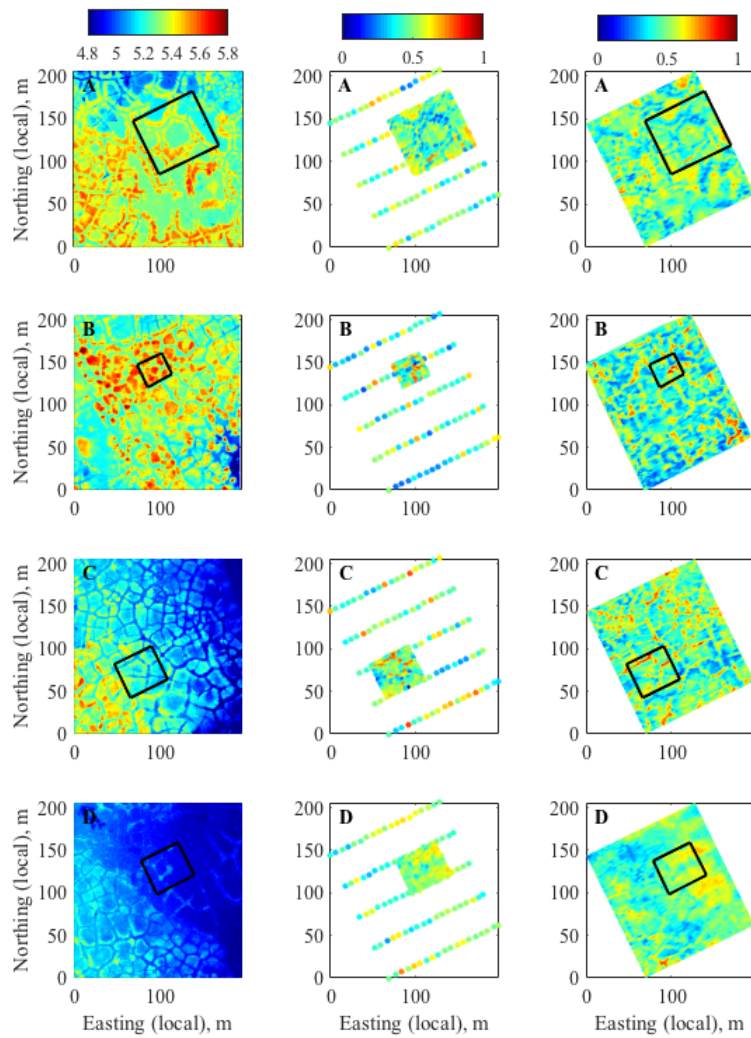


Figure 2. Radar velocity as a function of (a) co-located snow depth measured by a snow depth probe and (b) elevation difference (i.e., topographic variability) within 1 m. (c) Comparison between the probe-derived and GPR-derived snow depth at all the co-located locations (blue circles) and at selected locations (red circles) where topographic variability is low. In (a), the black vertical line is the median snow depth, and the dotted lines are \pm one STDEV from the median snow depth. In (b), the black line is the cut-off elevation difference of 0.05 m.



Deleted: point

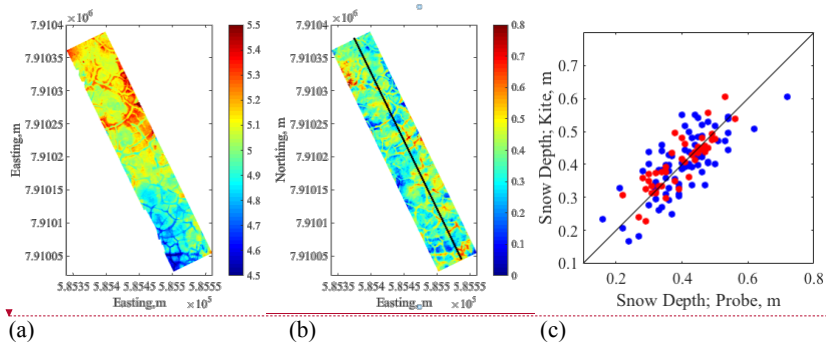
1317
1318
1319
1320
1321
1322
1323
1324
1325



1329
 1330
 1331
 1332
 1333
 1334

Figure 3. Elevation and snow depth in Plots A, B, C and D. The left column is LiDAR DEM (in meters), the middle column is the probe-measured snow depth (in meters), and the right column is the interpolated snow depth estimated using GPR (in meters). The black boxes represent the locations of the fine-grid snow depth measurements.

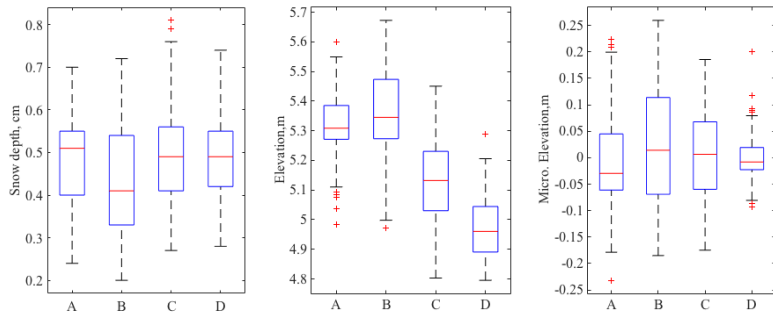
Deleted:



1336
 1337
 1338 Figure 4. (a) PhoDAR-derived DSM in meters (August, 2014), b) PhoDAR-derived snow depth
 1339 in meters (May, 2015), and (c) comparison between the PhoDAR-based and probe-based snow
 1340 depth at all the locations (blue circles) and at selected locations (red circles) having low
 1341 topographic variability (the sub-meter elevation variability less than 0.05 m). The black line in
 1342 (b) represents the snow depth probe measurements every 3 meter along the 500-meter transect.
 1343

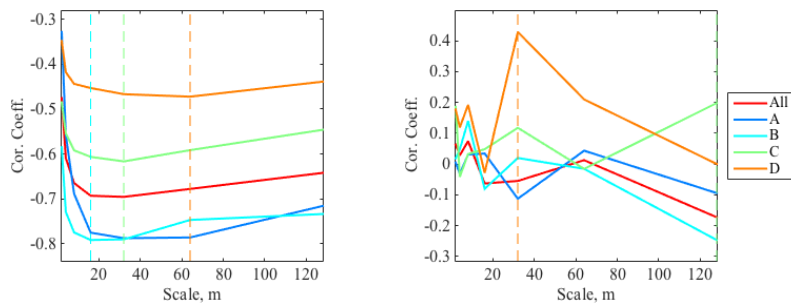
Deleted: [3]

Deleted: UAS
 Deleted: UAS
 Deleted: UAS



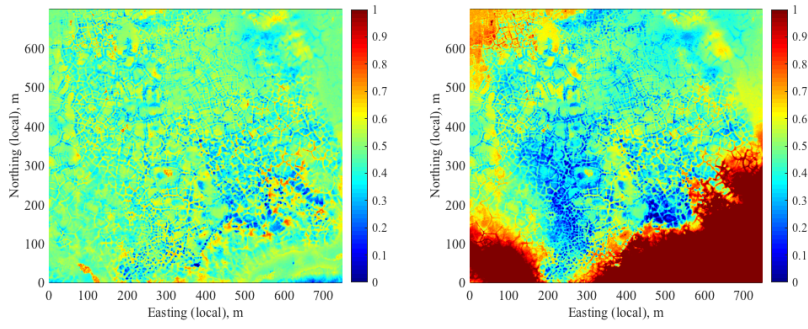
1349
 1350
 1351
 1352
 1353

(a) (b) (c)
 Figure 5. Boxplots of (a) snow depth and (b) elevation and (c) microtopographic elevation in Plots A-D.



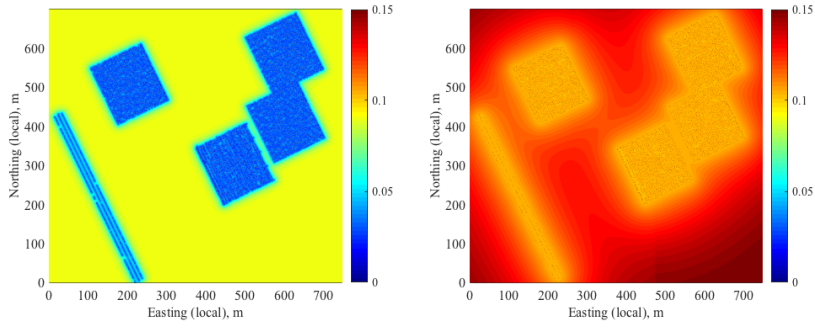
1354
 1355
 1356
 1357
 1358
 1359

(a) (b)
 Figure 6. Correlation coefficients between snow depth and topographic metrics as a function of the wavelet scale: (a) the microtopographic elevation, and (b) the wind factor of macrotopography. The different colors represent different plots (Plot A–D) or all the data (All). Each dash line represents the scale that maximize the magnitude of the correlation coefficient.



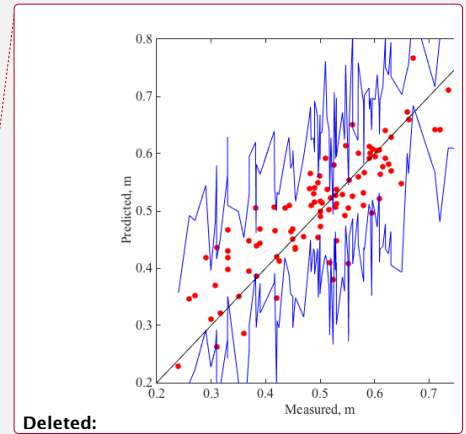
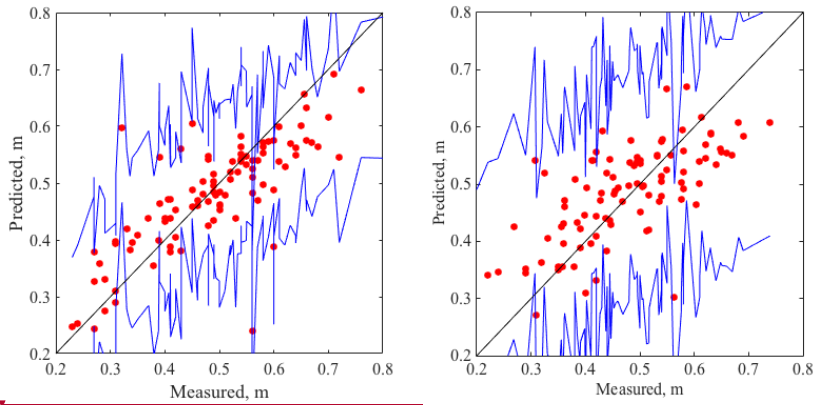
1360
 1361 (a) (b)
 1362 Figure 7. The estimated mean snow depth ~~over the NGEE-Arctic site~~ (in meters) based on (a) the
 1363 proposed Bayesian method including the correlation to microtopography, and (b) the kriging-
 1364 based interpolation of the snow surface. The spatial extent is the same as Figure 1b.
 1365

Deleted: across the site
 Deleted:



1368
 1369
 1370
 1371
 1372
 1373

(a) (b)
 Figure 8. The estimated standard deviation of snow depth across the site (in meters) based on (a) the proposed Bayesian method including the correlation to microtopography, and (b) the kriging-based interpolation of the snow surface. The spatial extent is the same as Figure 1b.



1374
 1375
 1376
 1377
 1378
 1379
 1380
 1381
 1382
 1383
 1384

(a) (b)
 Figure 9. Estimated mean and confidence intervals from the Bayesian method, compared to the probe-measured snow depth by (a) using the correlation to microtopography and (b) interpolating the snow surface. The red circles represent the snow depth at the validation locations (the [snow depth](#) probe measurements not used in the estimation), the blue lines are the confidence intervals based on the standard deviation (STD) multiplied by 1.9 (94% confidence intervals), and the black lines are the one-to-one line.

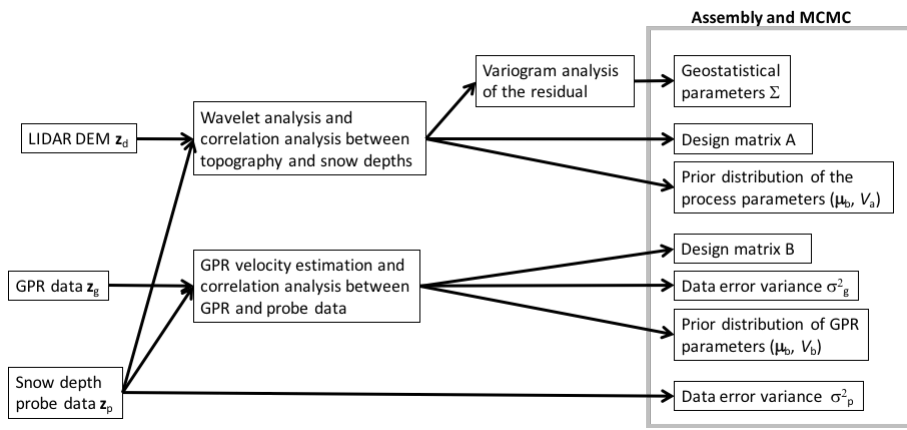


Figure B.1. Workflow of the Bayesian geostatistical estimation.

Deleted: .

1386
1387
1388
1389

1391 Table 1. Multivariate normal distribution defined for each variable.

Variable		Type	Distribution	Covariance	Mean vector
Snow depth	\mathbf{y}	Process model	$p(\mathbf{y} \mathbf{a}, z_d)$	Σ	$\mathbf{A}\mathbf{a}$
Probe data	z_p	Data model	$p(z_p \mathbf{y})$	D_p	\mathbf{y}
GPR data	z_g	Data model	$p(z_g \mathbf{y}, \mathbf{b})$	D_g	$\mathbf{B}\mathbf{y} + b_0$
Snow-depth parameters	\mathbf{a}	Prior	$p(\mathbf{a})$	\mathbf{V}_a	$\boldsymbol{\mu}_a$
GPR parameters	\mathbf{b}	Prior	$p(\mathbf{b})$	\mathbf{V}_b	$\boldsymbol{\mu}_b$

1392

1393 Table 2. Root mean squared error (RMSE) between the **PhoDAR**-derived DSM and **RTK DGPS**
1394 elevation measurements based on the three schemes: nearest neighbor, average, and minimum
1395 elevation within the 0.5 m radius.

Deleted: UAS

	Nearest (cm)	Average (cm)	Minimum (cm)
July 2013	6.88	6.41	6.62
August 2014	6.40	6.19	6.34

1396

1398 Table 3. p values from Tukey's pairwise comparison test for each pair of the plots.

	Snow depth
Plot A – Plot B	6.34×10^{-3}
Plot A – Plot C	0.982
Plot A – Plot D	0.998
Plot B – Plot C	1.72×10^{-3}
Plot B – Plot D	3.55×10^{-3}
Plot C – Plot D	0.997

1399
1400

1401 Table 4. Estimated geostatistical parameters and covariance models for snow depth, snow
1402 surface and residual snow depth.

	Model	Range (m)	Variance (m ²)	Nugget Ratio
Snow depth	Exponential	12.3	1.6×10^{-2}	0.0
Snow surface	Spherical	253.3	2.0×10^{-2}	0.16
Residual snow depth	Exponential	15.0	8.3×10^{-3}	0.0

1403

1404 Table A.1. Posterior distributions during the Gibbs sampling

Variable		Covariance, Q	Mean vector
Snow depth	\mathbf{y}	$(\mathbf{B}^T \mathbf{D}_g^{-1} \mathbf{B} + \mathbf{D}_p^{-1} + \Sigma^{-1})^{-1}$	$\mathbf{Q}(\mathbf{B}^T \mathbf{D}_g^{-1} (\mathbf{z}_g - \mathbf{b}_0) + \mathbf{D}_p^{-1} \mathbf{z}_p + \Sigma^{-1} \mathbf{A} \mathbf{a})$
Snow depth parameters	\mathbf{a}	$(\mathbf{A}^T \Sigma^{-1} \mathbf{A} + \mathbf{V}_a^{-1})^{-1}$	$\mathbf{Q}(\mathbf{A}^T \Sigma^{-1} \mathbf{y} + \mathbf{V}_a^{-1} \boldsymbol{\mu}_a)$
GPR parameters	\mathbf{b}	$(\mathbf{H}^T \mathbf{D}_g^{-1} \mathbf{H} + \mathbf{V}_b^{-1})^{-1}$	$\mathbf{Q}(\mathbf{B}^T \mathbf{D}_g^{-1} (\mathbf{z}_g - \mathbf{b}_0) + \mathbf{V}_b^{-1} \boldsymbol{\mu}_b)$

1405
1406

Figure 6. Correlation coefficients between snow depth and topographic metrics as a function of the wavelet scale: (a) the microtopographic elevation, and (b) the wind factor of macrotopography.